Lawrence Berkeley National Laboratory
LBL Publications

Title
Experimental and numerical investigation of proppant embedment and conductivity reduction within a fracture in the Caney Shale, Southern Oklahoma, USA

Permalink
https://escholarship.org/uc/item/2tg0p88f

Authors
Katende, Allan
Allen, Connor
Rutqvist, Jonny
et al.

Publication Date
2023-06-01

DOI
10.1016/j.fuel.2023.127571

Copyright Information
This work is made available under the terms of a Creative Commons Attribution License, available at https://creativecommons.org/licenses/by/4.0/

Peer reviewed

eScholarship.org Powered by the California Digital Library
University of California

Experimental and numerical investigation of proppant embedment and conductivity reduction within a fracture in the Caney Shale, Southern Oklahoma, USA

Allan Katende[1,2], Connor Allen[1,2], Jonny Rutqvist[3], Seiji Nakagawa[3], and Mileva Radonjic[1,2,4*]

[1*] Hydraulic Barrier and Materials Characterization Laboratory, 126, 127&130 Advanced Technology Research Center (ATRC),
Oklahoma State University, 420 Engineering North, Stillwater, 74078, Oklahoma, USA.

[2*] School of Chemical Engineering, Oklahoma State University, 420 Engineering North, Stillwater, 74078, Oklahoma, USA.

[3] Energy Geosciences Division, Lawrence Berkeley National Laboratory, 1 Cyclotron Road, Berkeley, 94720, California, USA.

[4] Boone Pickens School of Geology, Oklahoma State University, 420 Engineering North, Stillwater, 74078, Oklahoma, USA.

*mileva.radonjic@okstate.edu;

Abstract

The current worldwide energy supply is insufficient to meet the rising demand. As a result, energy prices are expected to keep soaring despite the recent increases in a variety of renewable energy resources.

Although not renewable, shale oil and gas— "unconventional" hydrocarbon resources—are relatively clean forms of energy resources that still hold a vast share of the energy market. For many oil and gas companies, meeting profitable production goals from shale reservoirs is sometimes challenging, due to the loss of fracture conductivity and premature declines in the production. In this paper we investigate the stress-dependent changes in the hydraulic conductivity of proppant-filled fractures and mechanical fracture-proppant interactions in Caney Shale, a calcareous, organic-rich mudrock, through laboratory experiments and numerical modeling. API fracture conductivity tests were conducted using 2% KCl on five locations within the Caney Shale that consisted of three brittle (reservoir) zones and two ductile zones. Confining pressures ranged from 1,000 psi to 12,000 psi at 210°F. Conductivity, permeability, and embedment were measured during the test. Additionally, a laboratory in-situ visualization test was conducted to examine the detailed proppant-shale matrix interaction under elevated stress (3,920 psi effective stress) and temperature (252°F), with a synthetic reservoir fluid. Our experimental results have confirmed that improved fracture conductivity is attributed to proppant size, and that the increase in porosity of the proppant pack, closure pressure changes, and the reduction in fracture conductivity are a function of many factors such as fracture closure stress.

Keywords: Energy Transition, Caney Shale, Computed Tomography, Fracture Conductivity, Fracture Permeability.

1 Introduction

During the last decades, unconventional shale resources have emerged as a substantial resource for natural gas contributing to the energy supply [1; 2; 3], sparking a global search for shale gas by energy corporations. Although there is a tremendous amount of reserves, most shale oil and gas can be accessed only via hydraulic fracturing, which introduces a long and conductive flow path that extends from a wellbore into the formation. In the created fractures, however, only the propped part is hydraulically effective, contributing to production. Hydraulic fracturing [4] is a procedure for enhancing formation permeability that improves hydrocarbon production from oil and gas-bearing formations. Proppant, which frequently consists of sand grains [4,5] of various shapes and sizes, is injected concurrently with the fracking fluid to disperse them throughout the rock fractures to keep the fractures open for hydrocarbon flow after the high injection fluid pressure is removed [6].

The material used as a proppant can range from naturally occurring sand grains to resin-coated ceramics [5]. When the frac fluid stops pumping, the proppant guarantees that the fracture does not seal [1]. A high fracture conductivity value is one indicative of a good fracture [5]. The width of the created fracture multiplied by the permeability of the supported zone equals fracture conductivity [7; 5]. The propped fracture has a significantly higher permeability than the surrounding formation, and it operates as a high permeability route for fluid flow, resulting in increased hydrocarbon production. API-RP19D; API-RP-19C[8; 9] criteria have been developed to assess how proppants will function in a fracture.

The proppants embed [5] into the formations due to their contact with the fracture surface under closure pressures, resulting in a reduction in fracture aperture and conductivity. In poorly cemented sandstones, shale rock, and coalbeds, proppant embedment plays a substantial role in reducing fracture aperture and conductivity [5; 6; 7]. Therefore, many reservoir and well-specific parameters—shale mineralogical composition, rock texture, chemical compositions of pore fluid and fracturing fluid, reservoir stress and temperature, drawdown pressure and schedule, and proppant properties—contribute to the overall performance of a hydraulic fracture.

The focus of this paper is on the effect of proppant embedment and confining stress on the conductivity of sand-propped fractures for the emerging Caney Shale in southern Oklahoma, USA. Previously, Katende et al.'s [10] experiments and modeling of Caney Shale indicated that substantial proppant embedment could occur and impact fracture conductivity for fractures containing a single layer of proppant ("monolayer" proppant). Also, it has been shown that creep could cause additional fracture compaction and fracture conductivity loss particularly for Caney units with high clay content, described as ductile units. In this study, we focus primarily on the conductivity of a fracture containing a multilayered proppant pack, the impact of stress, proppant embedment, and proppant crushing. A series of API fracture compaction tests are conducted on a multi-layered proppant pack between platens of various Caney shale units. Additionally, to examine the interaction between proppant grains and the shale matrix in detail, we conducted in-situ optical visualization of a model shale fracture (a "half" fracture) containing a sparse (~50% surface coverage) proppant monolayer. While such proppant monolayers can be expected to be prevalent in fractures away from the stimulation wells, multilayer proppant packs dominate in main stimulation fractures and provide for important connectivity between the well and a distant fracture network.

Finally, modeling was performed related to both proppant embedment and stress-dependent permeability of multilayered proppant packs as observed in the experiments

1.1 Literature review

The impact of fracturing is measured by fracture conductivity, which is influenced by parameters such as closure pressure, proppant size, and elastic modulus [5].

Many scholars [5] have published research on fracture conductivity experiments. To show the value of proppants, Fredd et al. [11] conducted experiments of hydraulic fracture conductivity. Their findings showed that in the absence of proppants, fracture shear displacement is essential for surface asperities to generate residual fracture width and adequate conductivity. The conductivity, on the other hand, can vary by at least two orders of magnitude depending on formation features such as fracture displacement, asperity size and distribution, and rock mechanical properties. Depending on the proppant concentration, proppant strength, and formation parameters, the conductivity can be proppant or asperity dominated in the presence of proppants, an important understanding since the conductivity varies greatly and is difficult to predict in asperity-dominated situations. Low quantities of high-strength proppant limit the impact of formation characteristics and create proppant-dominated conductivity. Conductivity tests with flat, parallel core faces typically overestimate the conductivity found with hydraulic fractures at standard proppant concentrations.

Wang and Elsworth [12] investigated the impact proppant distribution had on the development of hydraulic fracture conductivity, and their findings revealed that increased compacting stresses and evolving proppant embedment at the top of the settled proppant bed decrease the aperture and, over time, decrease the effectiveness of these highly conductive zones. Zheng et al. [13] looked at the crushing properties of several proppants and how they affected fracture conductivity. Their findings showed that accurate characterization of the particles obtained from a crush test can provide a quick and effective method for evaluating proppant pack permeability and fracture conductivity, as well as changes in these properties under various compressive stresses, without the requirement for complex conductivity tests. In practice, two ISO standards are often employed to assess the performance of proppant. To test permeability and fracture conductivity, the ISO 13502-5 standard [8; 9] uses a conductivity cell with proppant inserted between two fracture faces and fluid flowing through it. This test is typically performed over a duration longer than 50 hours.

During hydrocarbon production, reservoir pressure drops, effective stress rises, greater loads are imparted to proppant particles, and proppant embedment occurs. Proppant variables such as proppant size, type, distribution, whether mono- or multi-layer proppant pack, as well as reservoir rock features, are all important in determining the degree of conductivity reduction caused by proppant embedment in narrow fractures [5].

1.3 Contribution and novelty

In the literature over the last two decades, out of every 100 published articles from 1975 to 2022 on fracture conductivity, only 3% of these studies were conducted at reservoir temperature and pressure. In our experimental study, shale platens were selected from different locations within the four-inch core to capture heterogeneity, seen later in Fig 2(a). As seen from Fig 2(a). the two fracture walls being investigated are not identical as you can see samples are extracted from different locations along the core to capture heterogeneity. However, in other studies, they did not conduct experiments with platens that were from different parts of the four-inch core. Furthermore, our studies utilize fresh core specimens that

were extracted from a well drilled in 2020 as opposed to studies in literature that use core specimens from outcrops and in some cases cores that have been in storage for a number of years. In addition, fluids and proppants used in our study are obtained as samples from a field lab, which differ from synthetic fluids and proppants used by previous scholars. The confining stress was also varied in such a way that samples were tested to a maximum confining stress of 12,000 psi (83 MPa) and then slowly reduced to 6,000 psi (41 MPA) and 4,000 psi (28 MPa) to see whether permeability would be re-instated to its original value after a higher confining stress; however, the formation was already damaged with the higher confinement in stress.

2 Geological Area and Petrophysical Characteristics of the Caney Shale

The Ardmore basin, which has a northwest to southeast orientation, lies adjacent to the Arbuckle basin and is located in Oklahoma, USA [14]. Massive, precambrian granites dominate the Ardmore basin as a whole, have been dated isotopically to be between 1,050-1,350 million years of age, and belong to a vast continental craton [15]. The Paleozoic sediments that overlie them are sparse and have experienced little disturbance, only some general block faulting and slight faulting [16]. The Arbuckle basin lies to the north of Anadarko basin, while the Marietta basin and Arbuckle uplift are to the southeast and to the north and east, respectively [17]. The Admore basin emerged due to three significant tectonic events as detailed in the following: A three arm rift that occurred in the late Proterozoic to early Paleozoic first instigated the Protoatlantic Ocean's opening via two arms. After the failure of the other arm, the Southern Oklahoma Aulacogen (SOA) was formed [17; 18]. Next, a thick sedimentary sequence was deposited due to subsidence and the passive margin established by the aulacogen. Lastly, the Ouachita Oregeny emerged in the Pennsylvanian time during the collision between North America and Gondwana, producing major uplifts and basins that led to the Ardmore basin's current configuration [19]. Figure 1 shows geological basins within Oklahoma as well as the producing shale plays in Oklahoma. These encompass the Woodford shale, which consists primarily of the Mississippian shales containing a total organic content (TOC) greater than two percent (2%). According to Wang and Phillip [20] the Woodford shale, which is predominantly found in the Anadarko basin, is composed of mostly type II kerogen. The Caney shale, which is stratigraphically similar to the Fayetteville and Barnett shales, is thought to be type II-III kerogen, with a total organic content between one percent and twelve percent (1%-12%) and a 0.5% to 12% thermal maturity [21]. Kamann [22] did a comprehensive study of the Caney Shale from wells in the Arkoma basin and demonstrated that to the west of the basin, the Caney Shale was experiencing thickening. In the Arkoma basin, the Caney Shale wells have not been very productive, whereas Caney Shale wells drilled in the Admore basin demonstrated an improved production output for oil and gas [21].

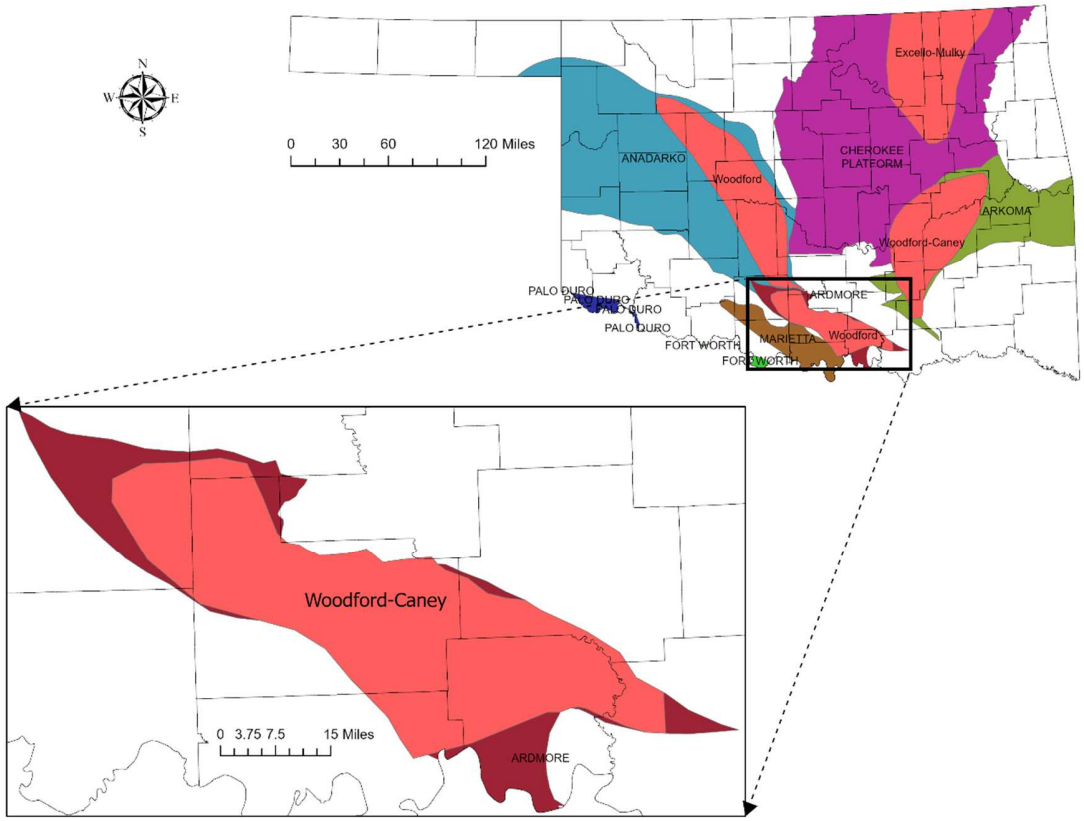

Fig. 1 Map showing location of the Caney Shale and geological basins in Oklahoma on the Oklahoma state map within the United States map. The bottom left corner shows Caney Shale within the Ardmore Basin, Oklahoma. The well in this study corresponds to a key location within the Ardmore Basin.

3 Methodology

3.1 Sample Preparation

This section presents a detailed description of sample acquisition and preparations needed to achieve the experimental methodology.

3.1.1 Shale samples

Caney Shale core samples were obtained from a Tomaney 1-35-34- 27XHW [23] well and used in this study. For the API conductivity tests, platens were cut to a size of 7in (177.8 mm) in length, 1.5in in width and 0.5in in thickness as presented in Figure 2. From one core, platens were obtained from different locations to pair up with a platen of similar formation to investigate heterogeneity. This is depicted in Figure 2(a), which shows how shale platens of 1.5-in by 0.5-in were extracted from a four-inch core sample that was retrieved from a well drilled in January 2020. For the in-situ visualization test, a thin, disc-shaped sample with a diameter of 1.75in (44.4 mm) and a thickness of 0.25 in (6.35 mm) was cored perpendicular to the bedding planes and stabilized in a stainless-steel ring with high-temperature epoxy, laid out in Figure 2(b).

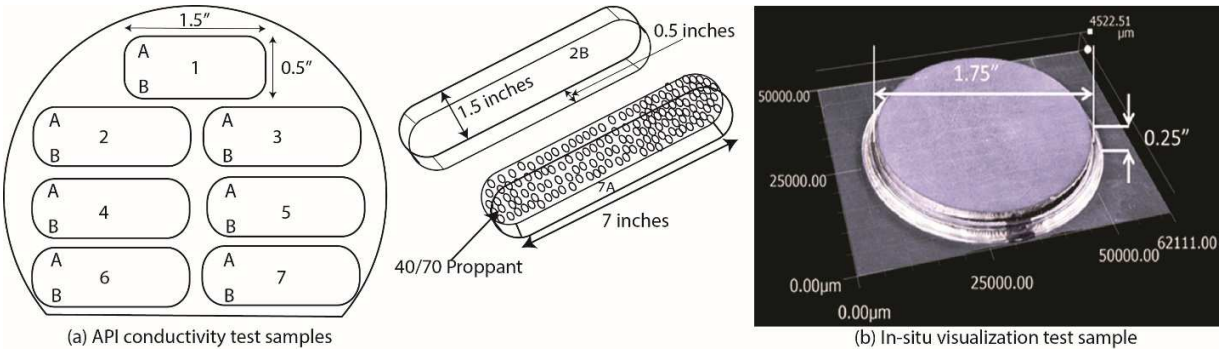

(a) API conductivity test samples

(b) In-situ visualization test sample

Fig. 2 Shale sample preparation for API conductivity tests (a) and for an in-situ visualization test (b).

Figure 2 shows how the samples used in this experiment were acquired. From figure 2(a), we can see how shale platens of 1.5-in by 0.5-in were extracted from a four-inch core sample that was retrieved from a well that was drilled in January 2020. Figure 2(b) shows a thin shaped disc sample with a diameter of 1.75in(44.4mm) and thickness of 0.25in (6.35mm) cored perpendicular to the bedding plane and stabilized in a stainless-steel ring with high-temperature epoxy. The disc was used for in-situ visualization tests discussed in this paper.

3.1.2 Proppant samples

In this experiment, 40/70 Northern white sand was used as proppant to conduct the API 19D fracture conductivity tests. This type of proppant was used in other publications, and it is frequently used as a standard proppant material [5].

3.1.3 Test fluids

Two percent potassium chloride aqueous solution (2%weight KCl) was used as the laboratory testing fluid in this experiment, which is an approximation of the hydraulic fracturing fluid frequently used by industry in API 19D tests.

3.2 Pre-Experiment Sample Characterization

The Caney drilled core was retrieved in January-February 2020 and was cleaned and slabbed by an industry laboratory in Oklahoma City. The core was available for viewing during a Caney project workshop held at Chesapeake's Reservoir Technology Center, in Oklahoma. At this time all project partners from academia, national lab, and industry discussed what areas of the core needed to be focused on in our research, based on core and various logs available at the time.

3.2.1 Computed Tomography (CT) Imaging

Before samples were cut, the cored 4in core sample was scanned using an industrial CT scan with a current of 200mA and a voltage of 135kV, and the data is available in Paronish et al [23].

3.2.2 X-ray Diffraction (XRD) Analysis

Twenty grams of samples from three selected depths were collected for powder XRD to identify and quantify mineral compositions. The powder XRD analysis was conducted using a Bruker D8 Advance XRD with Lynxeye detector. Before the XRD analysis, samples were dried at 105°C and ground to less

than 35 microns. Each sample was scanned from 5-80 degrees 2-theta with a 0.01-degree step and a dwell time of 0.5 seconds. Semi-quantitative XRD analyses were done using Rietveld Analysis. Tests were repeated multiple times and also obtained by different researchers for repeatability [24].

3.3 Proppant Embedment and Conductivity Tests

This section presented the methods used for assessing fracture conductivity tests as well as in-situ fluorescence visualization (ISFV) of fracture aperture distribution.

3.3.1 API-19D Fracture Conductivity Test

Long-term fracture conductivity and permeability testing was performed using an API fracture conductivity cell (Figure A1 in Appendix A), following the API-19D testing protocol, which are usually done at the pressures 2000-psi(13.79-MPa), 4000-psi(27.58-MPa), 6000-psi(41.37-MPa), 8000-psi(55.16-MPa), and 10,000-psi(68.95MPa) closure stress levels. The test was performed at a temperature of 210°F using a 2% KCl solution. The cells were reloaded at 2lb/ft^2 between Caney shale formation platens. American Petroleum Institute procedure (API-19D) [8] for measuring the long-term conductivity of proppants was used to obtain baseline values. Standard baseline testing is 50 hours at each stress level from 2000-psi (13.79-MPa) to 10, 000 psi(68.95-MPa).

To enable the proppant-rock sample to acquire a semi-steady state condition, a 1,000-psi closure stress is applied across a test unit for 12-24 hours at a reservoir temperature, in the case of Caney formation it is ~125°C. The stress level is subsequently raised to the required level and held for 50 hours. The pack width, differential pressure, temperature, and flow rates are assessed at each stress as the fluid is flowed through the proppant bed. Proppant pack permeability (Equation 1) and conductivity (Equation 2) are then calculated from Darcy's equation as shown below.

$$K = 321.4\frac{\mu Q}{(\Delta P)Wf} \quad (1)$$

$$k_{Wf} = 26.78\,\frac{\mu Q}{(\Delta P)} \quad (2)$$

Where:

- k is the proppant pack permeability in Darcy
- kWf is the proppant pack permeability in mD-ft
- μ is the viscosity in cp
- Q is the flow rate in cm3/s
- ΔP is the differential pressure in psi
- Wf is the proppant pack width in inches

3.3.1.1 Proppant pack width determination

By building the conductivity cell without the sample proppants, it is possible to determine the zero width of the proppant pack. At each of the four corners, the length between the width bars attached to each end of the conductivity cells is measured and recorded. After that, the cells are disassembled and reassembled with the proppant samples. The measurements are retaken at the start and end of each stress session (Figure 3). The average of the zero is subtracted from the average of each of the width values measured at each stress loading to calculate the width.

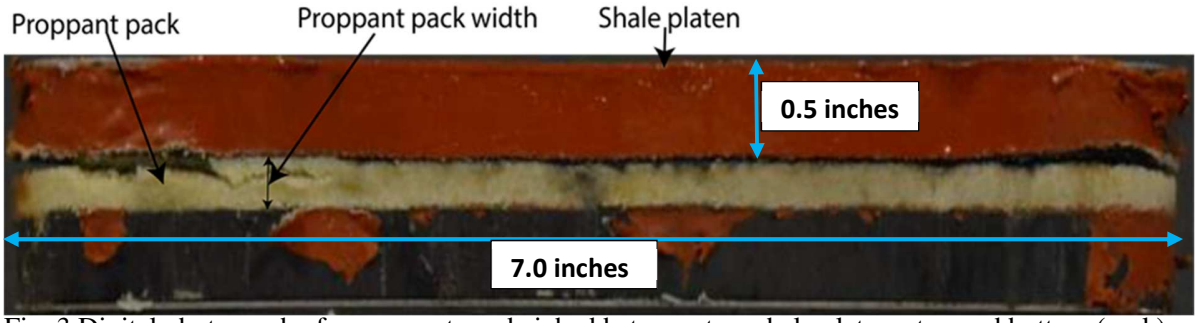

Fig. 3 Digital photograph of a proppant sandwiched between two shale platens, top and bottom (rock) and the 40/70 northern white sand proppant pack shown in the middle in lighter color.

3.3.2 In-situ fluorescence visualization (ISFV) of fracture aperture distribution

A long-term in-situ visualization experiment was conducted using a half-fracture sample consisting of the sample shown in Fig.2b and a 0.5-in (12.7 mm) thick transparent sapphire disc, mediated by a sub monolayer of proppant covering approximately 50% of the sample surface. The schematic illustration of the equipment is illustrated in Figure A3 and Figure A4 in Appendix A. The proppant used in this experiment was round UNIMIN silica sand with grain diameters of 1.0-1.5 mm (14/18 mesh size). The fluid used in this experiment was synthetic brine with the fluid chemistry (NaCl 4.70wt%, $MgCl_2 \cdot 6H_2O$ 0.168wt%, $CaCl_2 \cdot 6H_2O$ 0.076%, SrCl2$\cdot 6H_2O$ 0.028%) based upon reservoir-produced fluids from one of the nearby wells.

The shale and sapphire discs and the proppant were pressed against a 1.0-in (25.4 mm) thick sapphire view window of a uniaxial compaction cell (Appendix Figs. A3 and A4). During the experiment, the sample was first saturated by percolating the brine across the disc thickness by applying a differential pressure of 0.35 MPa, under a compaction stress of 1.35 MPa at room temperature for seven days. Subsequently, the temperature was raised to 122˚C, and the pore pressure was elevated to 10.35 MPa. After 15 hours, the effective stress was increased to 27 MPa, and the fracture was compacted over two weeks.

To visualize the fracture and the proppant during the fracture compaction test, an optical imaging technique previously used by Nakagawa and Borglin [25] was used. This method involves introducing a green Ultraviolet fluorescent dye (WATER-GLO® 802-P, Spectroline) into the brine. The concentration of the dye used for this experiment was 0.1 wt%. UV light was introduced into the test cell through the view window, and the resulting fluorescence images were captured by a digital camera through a green, narrow-band filter (Baader, bandwidth=5 nm, center wavelength=540 nm)

3.4 Post-Experiment Characterization

This section presents methods used in a post experimental analysis of different parameters. These methods include, Scanning Electron Microscopy (SEM) analysis, sieve analysis, and surface profilometry.

3.4.1 Scanning Electron Microscopy (SEM) Analysis

Scanning electron microscopy was carried out using an FEI Quanta 600 field-emission gun Environmental Scanning Electron Microscope as shown in Figure A2, in both secondary electron mode and in the backscattered electron mode. The elemental mapping and spot mode analysis were obtained using a Bruker EDS X-ray microanalysis system. Images, maps and spectra were obtained at 20KeV, and various magnifications, from a larger field of view to a higher magnification revealed characteristics of interfaces and surface properties of various rock components, as well as embedded proppants.

3.4.2 Sieve Analysis

Sieve analysis was performed using the procedure found in API-RP-19C [9]. Standard US mesh screens are used to separate the samples by size. Based on the recommended sieve stack for a given proppant size, not more than 0.1% should be greater than the first specified sieve and not more than 1% should be retained in the pan. There should be at least 90% retained between the specified screens for an API graded proppant.

3.4.3 Surface Profilometry

Proppant was removed from the samples, which were then placed under a microscope and laser profiled to quantify proppant embedment. To gain more insight into proppant embedment, a Leica DVM9 Digital microscope was used to capture 2D and 3D scans. The Las X software used 3D scans to create topographical heat maps of the depth of the test sample and line profiles were then drawn to determine the height and depth of the proppant embedment.

3.7 Numerical Modeling

The goal with the numerical modeling is to develop and calibrate a model for stress-dependent fracture conductivity that can be applied for modeling the reservoir scale multiphase fluid flow and geomechanical processes during hydrocarbon production. The field scale production modeling is based on linking the TOUGH2 multiphase fluid flow simulator with the FLAC3D geomechanical simulator [26; 27; 28; 29]. In this study, we apply the simulators for modeling compaction of the proppant pack and associated changes in fracture conductivity. Because the 6 mm proppant pack contains several thousands of sand grains of various sizes, we are not able to model particles explicitly. Instead, the proppant pack is modeled as a continuum using a mechanical constitutive model that implicitly considers grain rearrangements and grain crushing. For this purpose, we applied the Modified Cam-Clay (MCC) constitutive model from soil mechanics [30]. The MCC model is applied in this case because it can handle plastic pore-collapse due to high compaction stress. It is applied here because of its relative simplicity as a model that has been applied in the past to model reservoir compaction (e.g. Chang and Zoback [31]). In addition to proppant-pack modeling, modeling of proppant embedment is performed at the scale of single proppants using a modeling approach previously applied in Katende et al. [5]. The shale was simulated using a Mohr-Coulomb plasticity model that has previously been demonstrated to be adequate to model elasto-plastic proppant embedment [10,32]. Modeling was first performed at the proppant scale to analyze the

embedment depth as observed from surface profilometry. Thereafter, modeling of the fracture conductivity tests were conducted to analyze the stress-dependent conductivity of proppant-filled fractures. These two aspects of modeling, the continuum modeling of the proppant pack compaction and proppant embedment, are presented in subsections 4.7 & 4.8.

4 Results

Results in this section are presented to begin with computed tomography image analysis, followed by mineralogical analysis, Scanning Electron Microscopy (SEM) Image Analysis, Fracture Conductivity (API 19-D) Testing Analysis, Particle Size Analysis, Laser Surface Profilometry and Proppant Embedment Quantification, In-situ fluorescence visualization (ISFV) of fracture aperture distribution, proppant embedment modeling and finally fracture conductivity modeling.

4.1 Computed Tomography (CT) Image Analysis

Before any experiment was conducted, CT scans were conducted to see what micro-structural differences existed in the selected samples. Figure 4 shows two 2D isolated planes through the vertical center of the 4-inch core samples. The samples were scanned using an industrial CT scanner from NETL [23] at a sub-millimeter core-scale resolution (91μm × 91μm × 100μm). Bedding planes, pyrite and micro-fractures are seen in all the samples. However, ductile samples had more visible micro-fractures compared to reservoir samples. This is because ductile samples have more clay content and are more fissile in nature compared to reservoir samples.

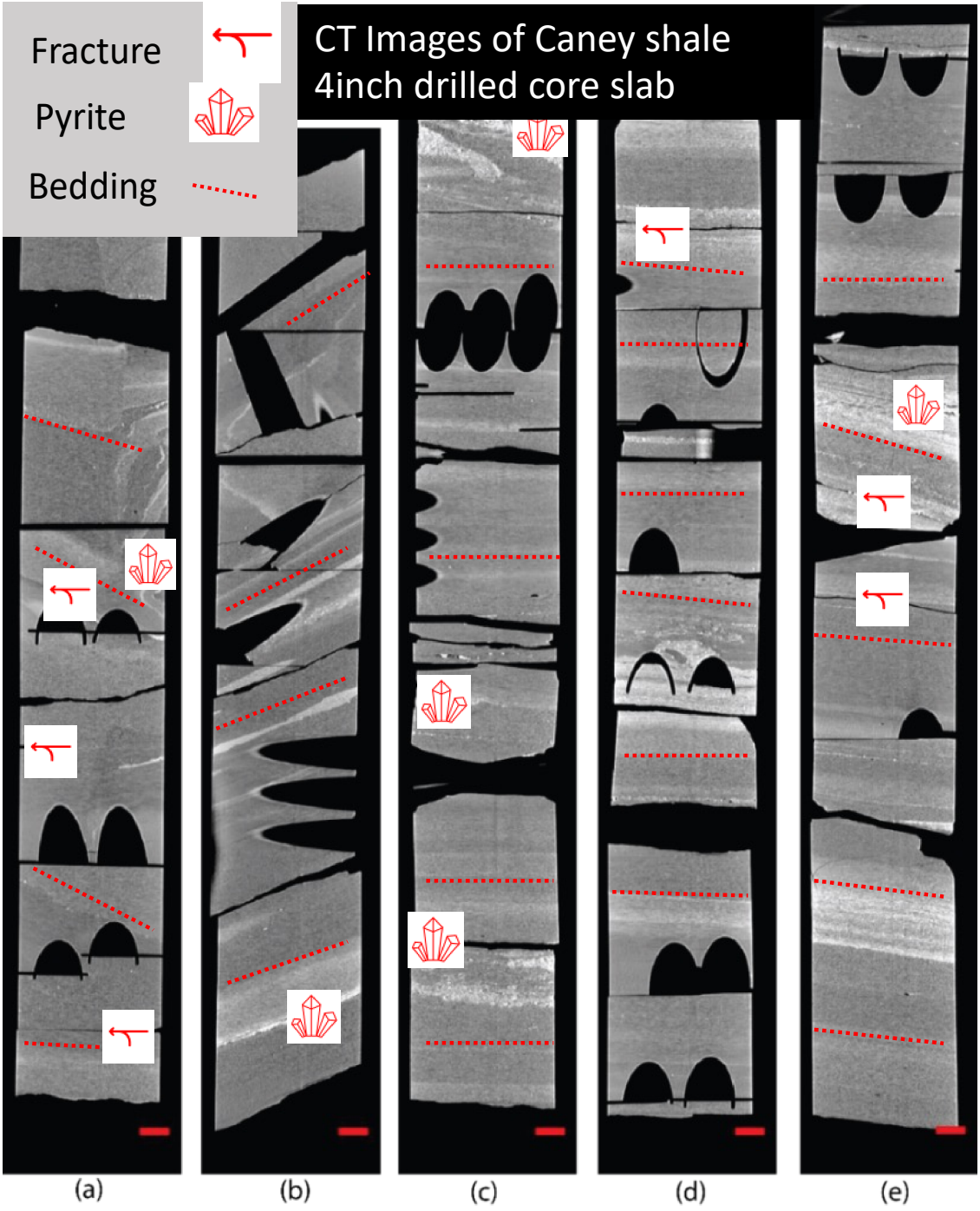

Fig. 4 2D isolated planes through the vertical center of the medical CT scans of the 4-inch core sample from which a part was used for API analysis and part was used to extract 1×2-inch core plugs at different orientations. (a) Reservoir 1 region. (b) Ductile 1 region. (c) Reservoir 2 region. (d) Ductile 2 region. (e) Reservoir 3 region. CT scans were conducted using an industrial CT medical scanner from the National Energy Technology Laboratory (NETL) [23].

4.2 Mineralogical composition (XRD) Analysis

X-ray diffraction (XRD) was conducted to understand the composition of the rock fabric. Figure 5 presents results of mineralogy using a powder X-ray diffraction analysis. From Figure 5, Quartz is the most abundant mineral and ranges from 39% in Reservoir 3 to 64% in Reservoir 1. The most striking difference in the results obtained is that the ductile samples have double the number of clays compared to the reservoir samples.

Radonjic et al. [33] noted that the higher the clay mineral content, the more ductile the sample is whereas a lower clay mineral content indicates brittleness. Holt et al.[34], defined the brittleness behavior in shales as the opposite to ductility and occurs when a rock is deformed after failure, there is a lack of irreversible deformation and a loss of load bearing capacity. Whereas in a ductile rock, the rock could be deformed with an increasing or declining ability to carry a load which doesn't facilitate the initiation and propagation of fractures.

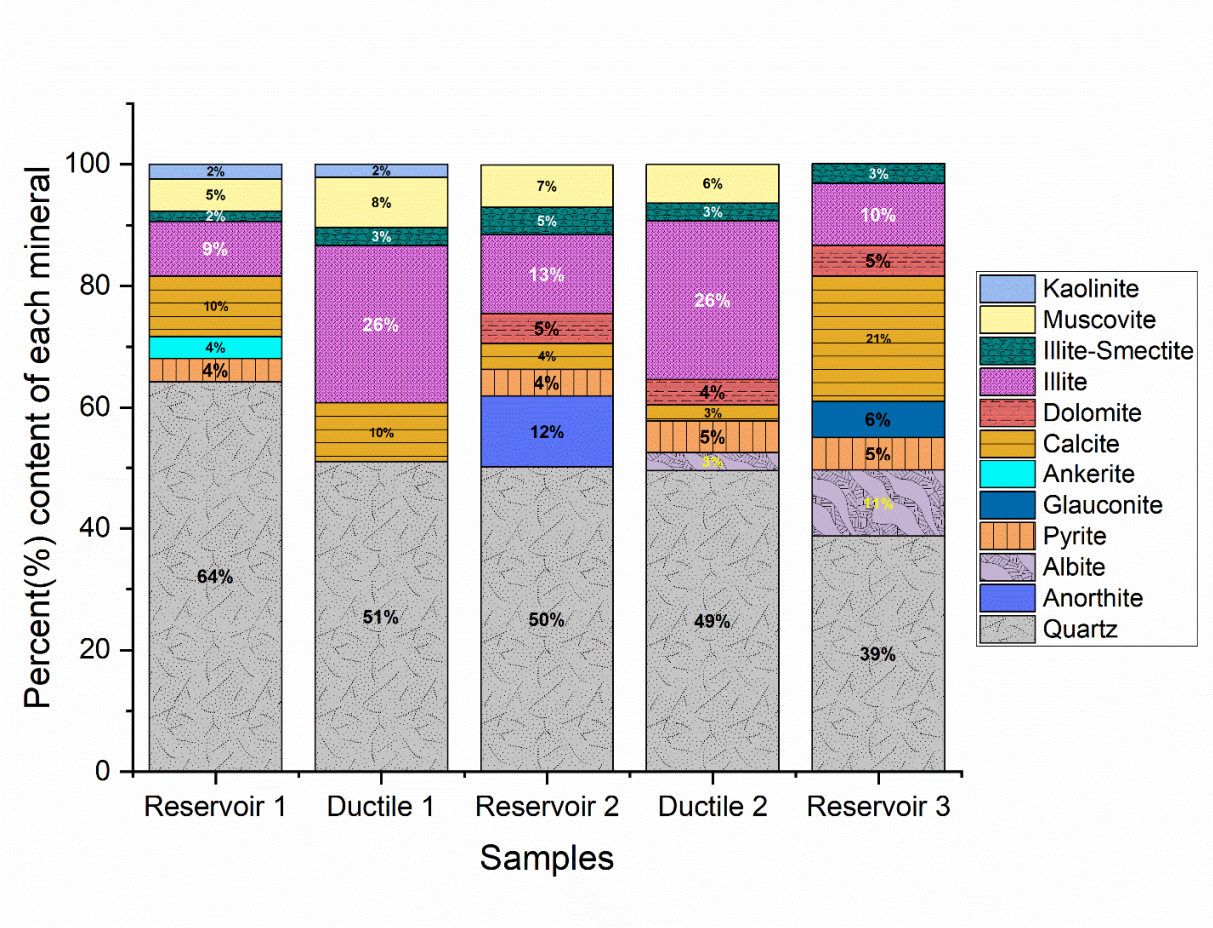

Fig. 5 Mineral composition from each Caney section identified as reservoir or ductile.

4.3 Scanning Electron Microscopy (SEM) Image Analysis

Figure 6 shows scanning electron micro-graphs conducted on the five test specimens used in this study. From it, we can see a spatial distribution of organic matter alongside pores. Natural fractures, pyrite, inter-particle organic matter and intra-particle organic matter are seen in the SEM micro-graphs. Clays being closely packed together are seen in the SEM micro-graphs.

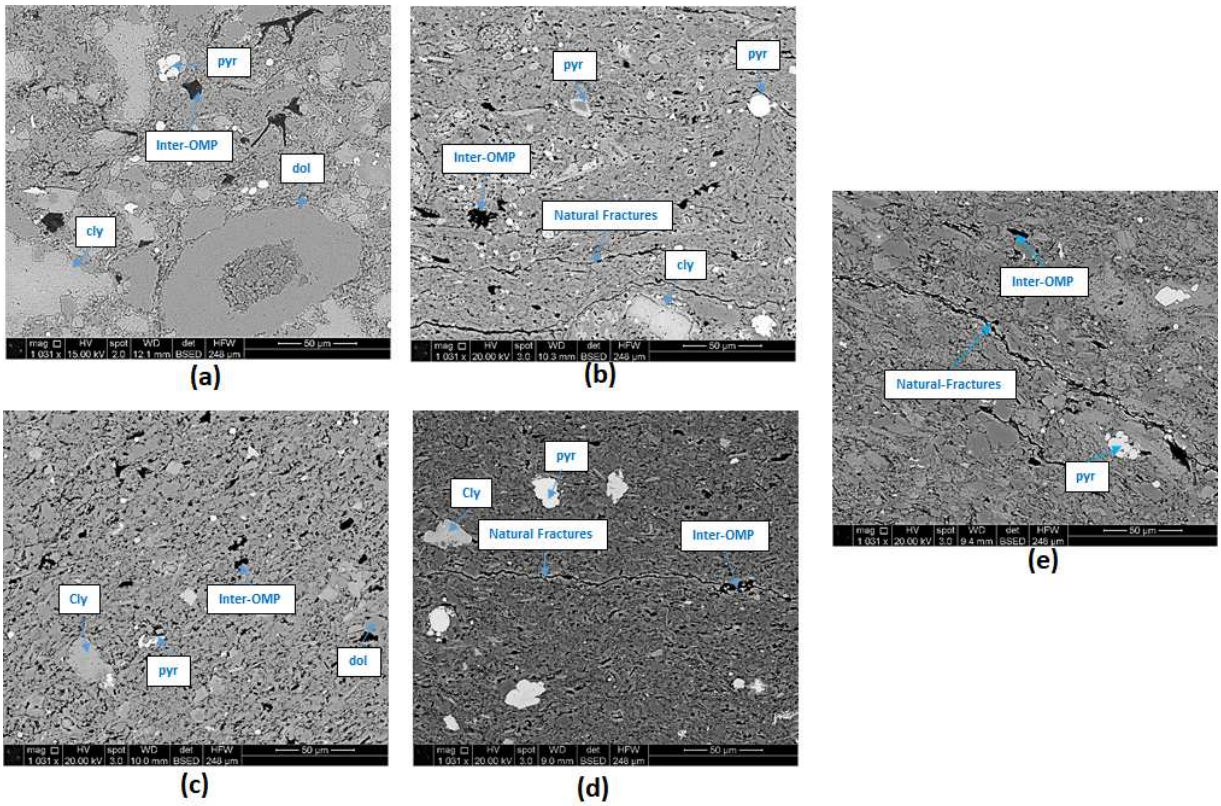

Fig. 6 Scanning Electron Microscopy Analysis of the selected samples: (a) Reservoir 1; (b) Ductile 1; (c) Reservoir 2; (d) Ductile 2; (e) Reservoir 3

4.4 Fracture Conductivity (API 19-D) Testing Analysis

Fracture conductivity is important for successful production of oil and gas from reservoirs. Figure 7 presents results of fracture conductivity versus closure pressure. Figure 8 presents the permeability versus closure pressure. From Figure 7 and Figure 8, we can see that the conductivity and permeability is higher for the 40/70+Reservoir 3-2, 2B&7A sample compared to all other samples. As the closure stress increases, the fracture conductivity and fracture permeability decrease for all samples due to compaction of the proppant pack as more stress is applied over time. This is because as more stress is applied, the formation begins to become more closely-packed as is indicated by the sharper decline up to 12,000 psi. Figure 9 shows fracture width versus stress for all the samples tested. Width shows a sharper decline for all the samples up to 12,000 psi closure stress. The non-close packing arrangement of the 40/70 proppant created higher conductivity and permeability at a lower stress than the base proppant, but after 12,000 psi the proppant pack widths are constant for the Ductile 2-1, 2b&7A, Reservoir 3-2, 2B&7A. The decline in conductivity and permeability shown in Figures 7& 8 at very low closure stresses without proppant embedment are due to the compression of the proppant pack and thus a decline in the path porosity. Much and Penny [35] studied the performance of proppants under simulated conditions and their work involved

determining porosity from the width equation. They noted that the production from hydraulically fractured wells was dependent upon the ability of the propped fracture to transmit reservoir fluids. However, in the presence of proppant embedment such as what we see in Figures 13, & 14, the alone fracture width decrease shown in Figure 9 may not predict the change in permeability and porosity and the issue of spalling must then be considered. Spalling is the extrusion of core-face fines into the proppant pack. The fines are generated by the embedment process, so the degree of spalling loss is associated with the depth of embedment. It is also described in terms of proppant mean grain diameters. The internal pack width, or the width of the pack channel open to flow, is the external pack width minus spalling and filter cake losses.

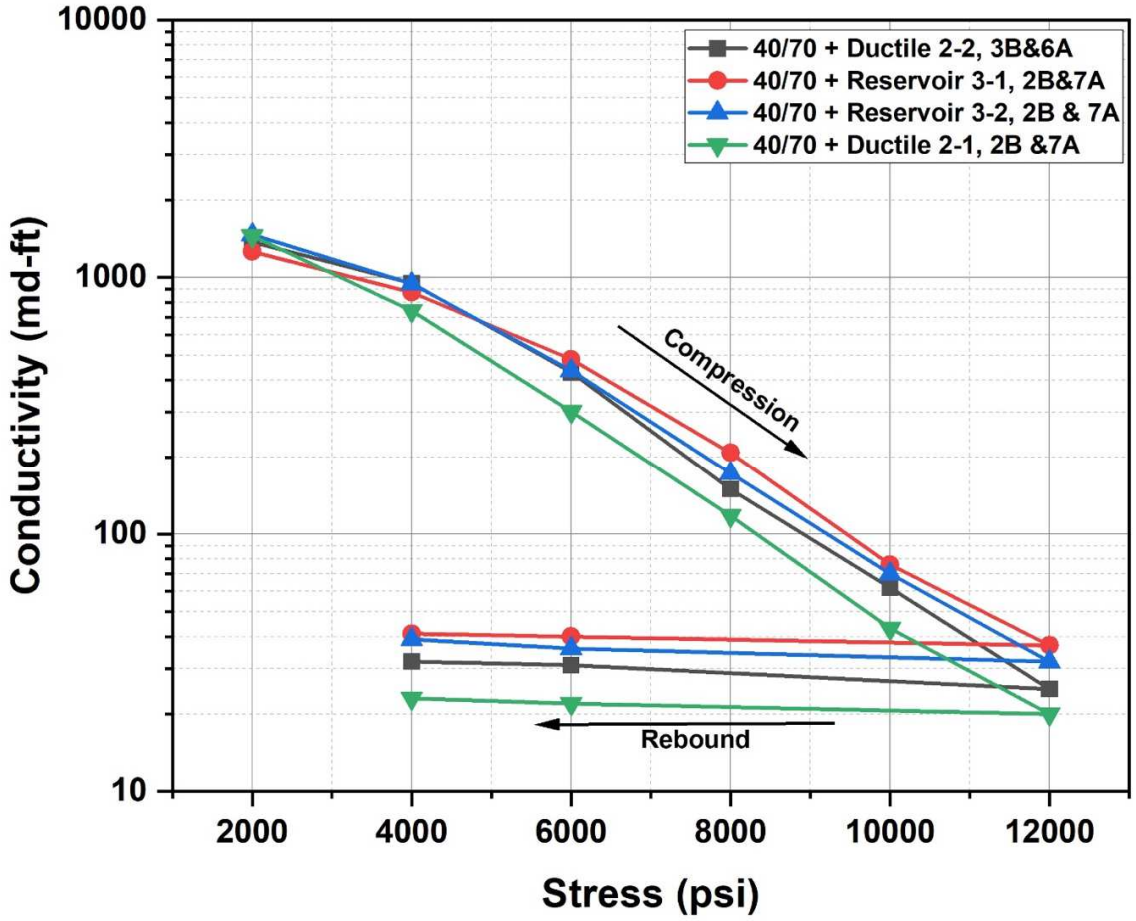

Fig. 7: A plot of fracture conductivity versus confining stress for the Ductile 2-2 3B&6A, Reservoir 3-1, 2B&7A, Reservoir 3-2, 2B&7A and Ductile 2-1, 2B&7A with 40/70 as proppant. Data is presented in table A1 in Appendix B

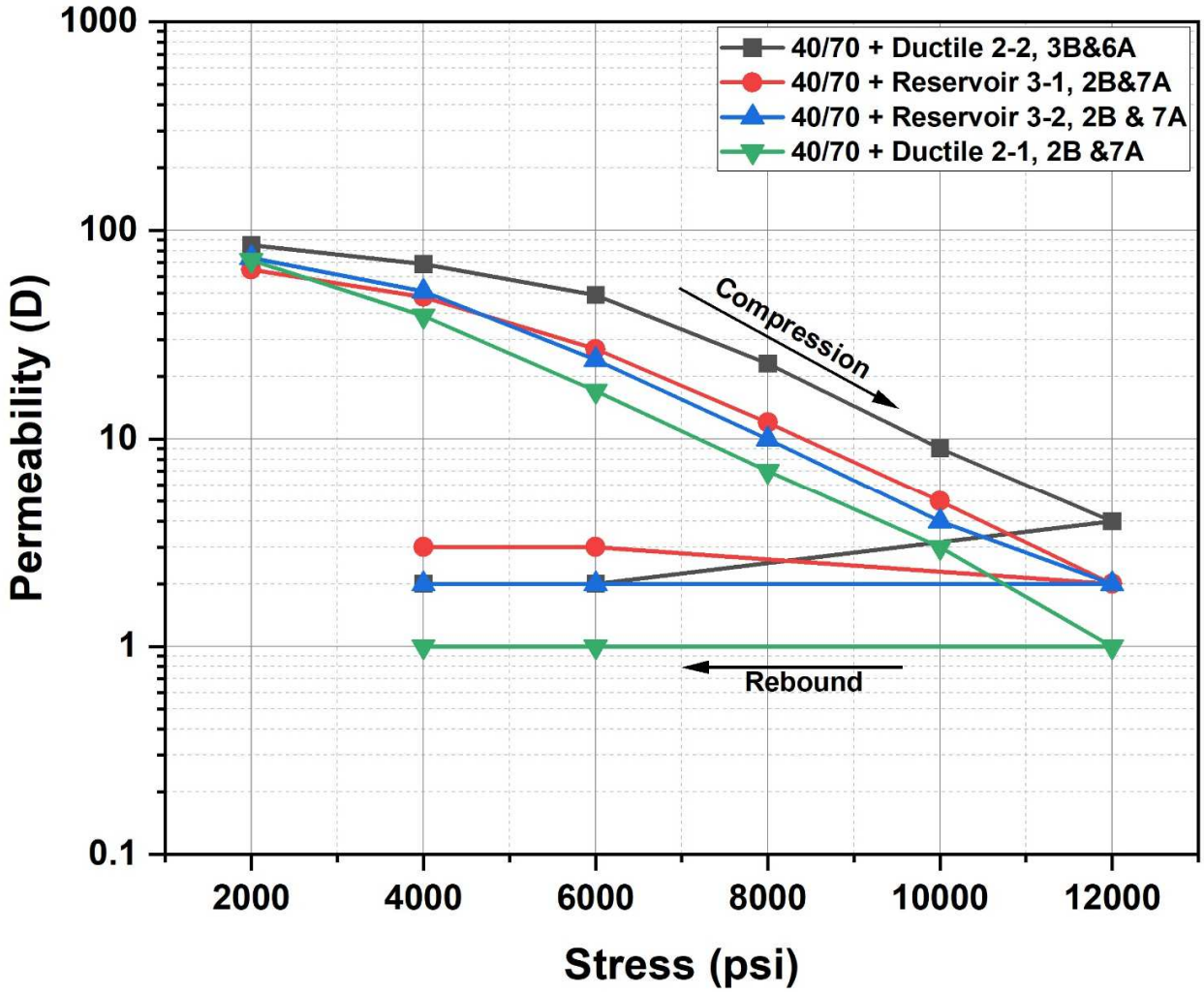

Fig. 8 A plot of fracture permeability versus confining stress for the Ductile 2-2 3B&6A, Reservoir 3-1, 2B&7A, Reservoir 3-2, 2B&7A and Ductile 2-1, 2B&7A with 40/70 as proppant. Data is presented in table A2 in Appendix B

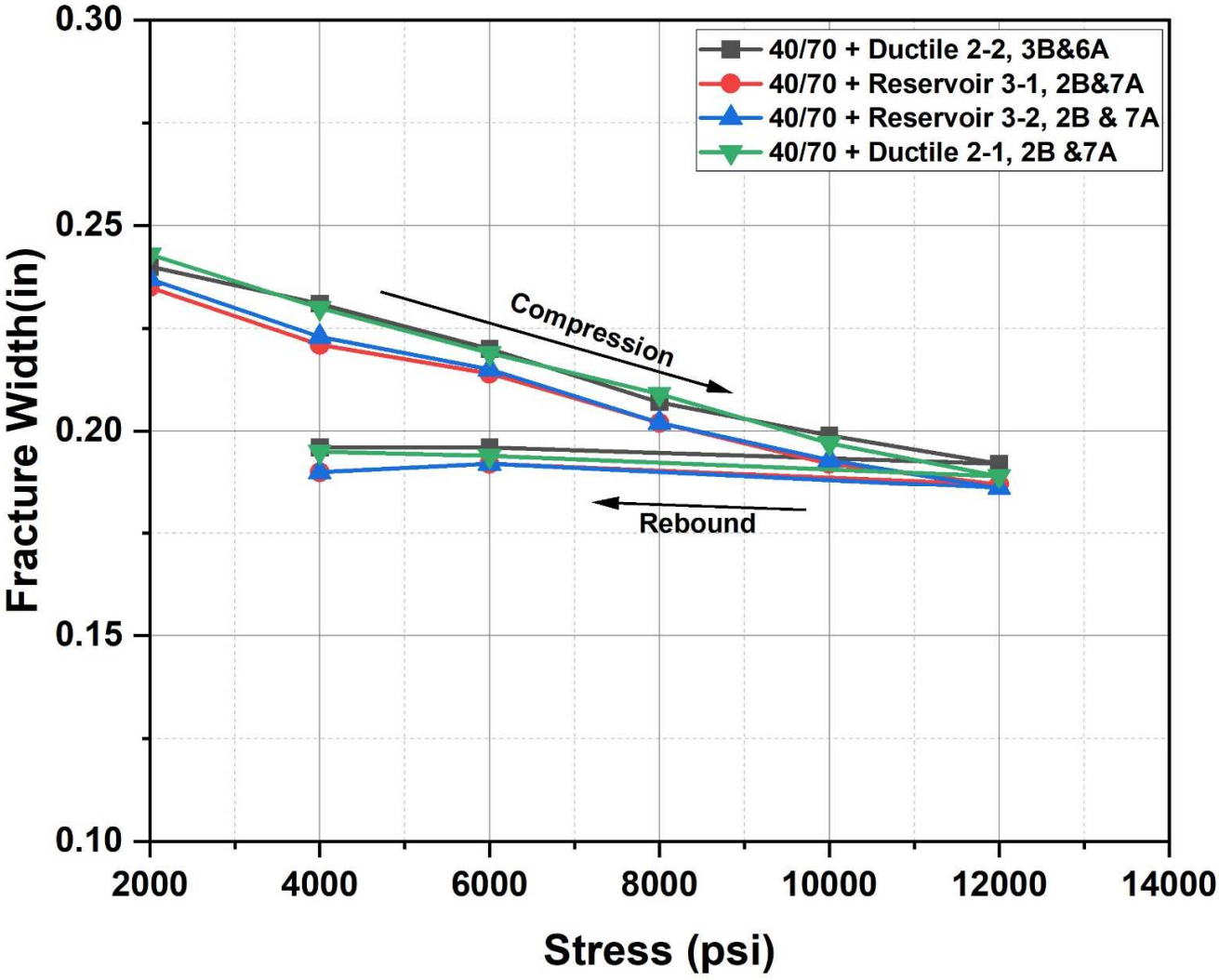

Fig. 9 A plot of fracture width versus confining stress for the Ductile 2-2 3B&6A, Reservoir 3-1, 2B&7A, Reservoir 3-2, 2B&7A and Ductile 2-1, 2B&7A with 40/70 as proppant.

4.4.1. Statistics of proppant embedment from this experimental study

In order to assess the effect of proppant embedment between reservoir and ductile samples. Laser surface profilometry linked to a Raman microscope was used to investigate this effect. Figure 10 shows the illustration of the shale platen surfaces for both reservoir and ductile after the fracture conductivity tests. From these results, we can conclude that ductile samples experienced severe proppant embedment as compared to reservoir samples. This is particularly because ductile samples have a higher clay content compared to reservoir samples and, due to this, the percentage of proppant embedment in ductile samples was much higher compared to reservoir samples as seen in Figure 10. In other words, from the area that was surface profiled, more than 60% of the surface was damaged in ductile samples as compared to reservoir samples.

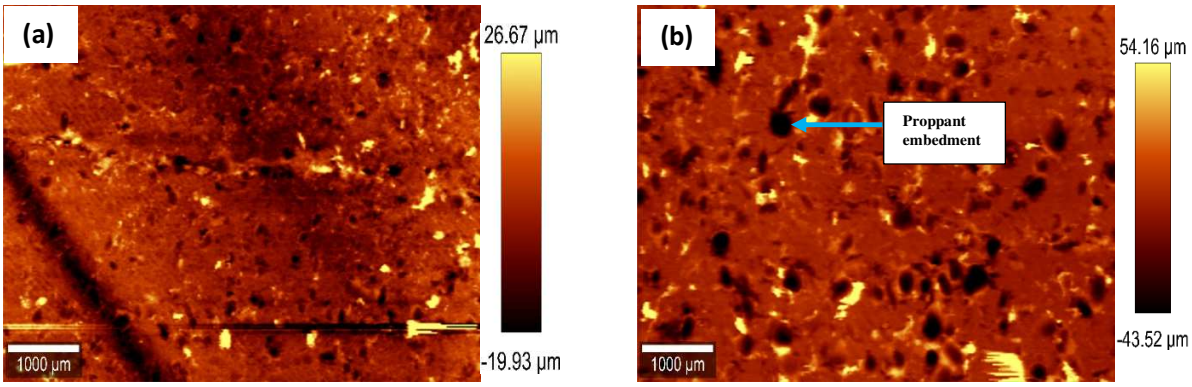

Fig. 10. Illustration of surface profilometry obtained by Raman spectroscopy of shale platens after fracture conductivity testing; (a)surface of shale platen on a reservoir sample after test (b) surface of shale platen on a ductile sample after test.

4.4.2 Particle Size Analysis

Figure 11 shows a plot of particle size analysis after an API test was conducted indicating the percentage of proppant retained using different US mesh sizes. The sieves help quantify the amount of proppant that has been crushed after the experiment and compare these to the original proppant sizes. When describing proppant, it is frequently referred to as a sieve cut, and the shape of proppant is important because the shape and size influence the final permeability through the fracture. A smaller sieve cut after the test indicates severe fracture conductivity damage. The conclusion drawn from Figure 11 is that the combined effects of proppant crushing against formation strength plus the rock fluid interactions at different temperatures and pressures also plays a significant role in fracture conductivity. These observations are also similar to studies conducted by recent researchers [5].

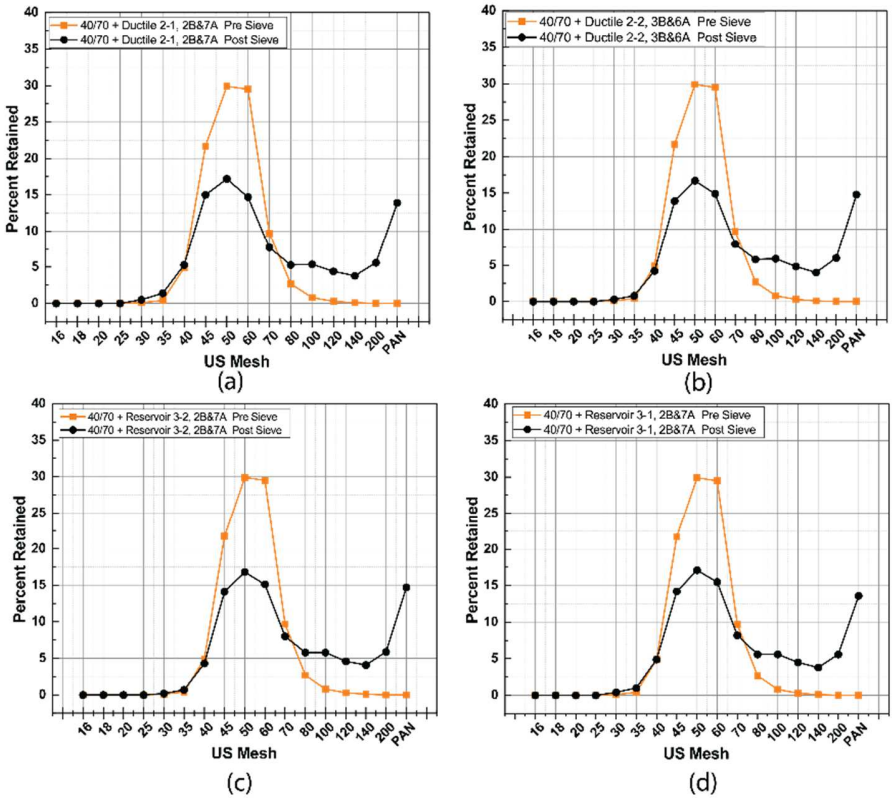

Fig. 11 A plot of particle size analysis showing the percentage retained versus different US mesh sizes for (a) 40/70 + Ductile 2-1, 2B&7A. (b) 40/70 + Ductile 2-2, 3B&6A. (c) 40/70 + Reservoir 3-2, 2B&7A. (d) 40/70 + Reservoir 3-1, 2B&7A. Data is presented in table A3 in Appendix B.

4.5 Laser Surface Profilometry and Proppant Embedment Quantification

Figure 12 shows the top view of the Ductile 2-2, 3B& 6A shale platens that were used for fracture conductivity analysis. Figure 13 shows the optical micrographs revealing embedment imprints for the Ductile 2-2 6A inlet and Reservoir 3-1 7A inlet. Figure 14 shows the surface profiles conducted on the shale platens. Embedment losses grow considerably for softer rocks. Pack width loss to embedment can approach one full grain diameter or more on each face for nearly unconsolidated sands [36]. It is impossible to calculate width loss due to embedment because it can't be seen without disassembling the proppant pack. It impacts both available flow breadth and conductivity, as well as internal fluid velocity in the pack. Its effects can often be attributed to a reduction in permeability and other times to a shift in pack width. Internal width losses and how they are treated can have a big impact on velocity-dependent (non-Darcy) conductivity estimates. Figure 14 also depicts a second source of effective pack-width loss that is not as visible from the outside: The loss of width caused by the formation spalling into the proppant pack. The ejection of formation material into the proppant pack is known as spalling. Crushed formation grains or fines are typically created during the embedment process as the tougher proppant grains are driven into the fracture wall. Proppant embedment and width loss owing to stress, which is dependent on reservoir rock qualities, both result in permeability loss, while spalling causes further width loss, which leads to permeability degradation.

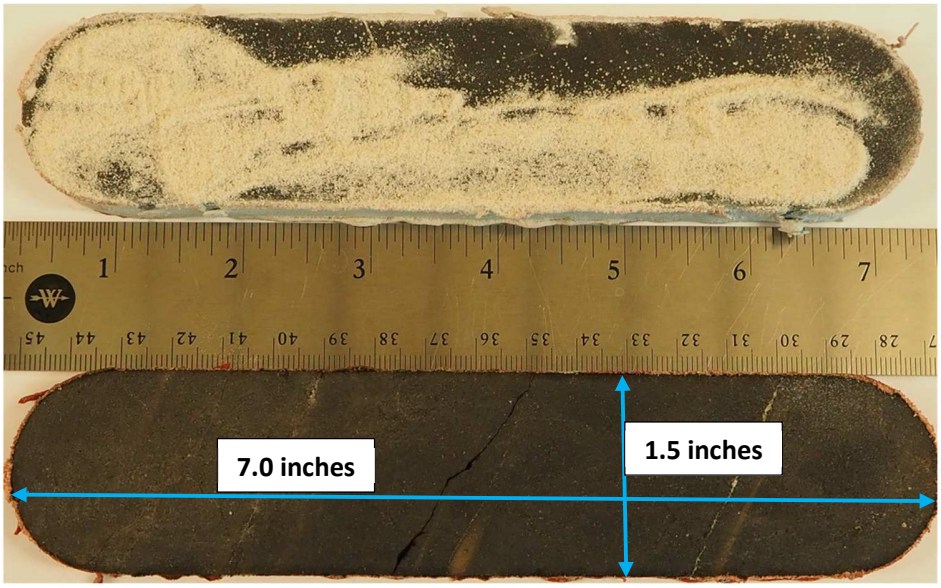

Fig. 12 Top view of 40/70 + Ductile 2-2, 3B & 6A sample proppant pack.

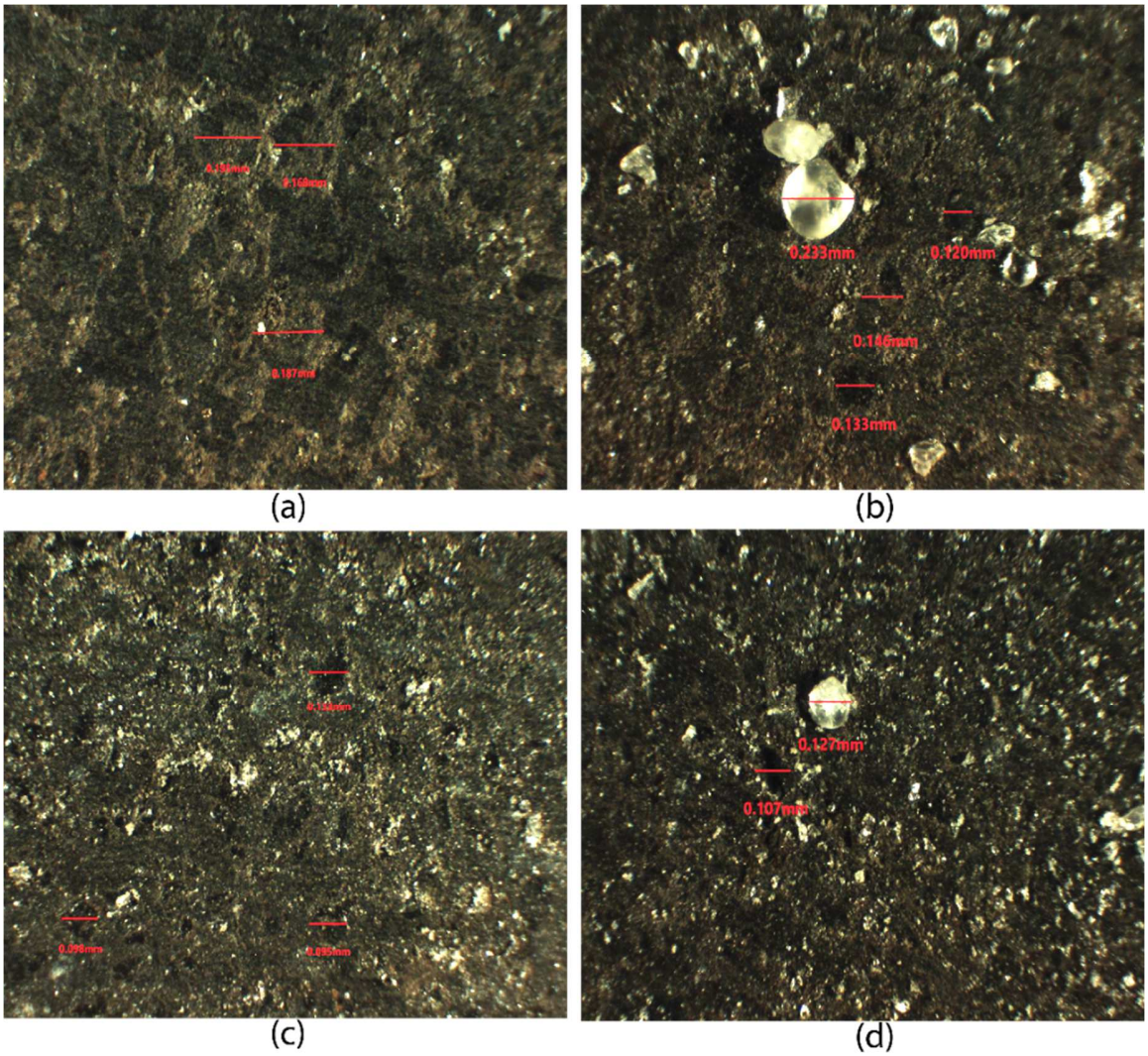

Fig. 13 Optical micrographs showing embedment imprints on the: (a)&(b)40/70+Ductile 2-2, 6A Inlet. (c)&(d)40/70+Reservoir 3-1, 7A Inlet

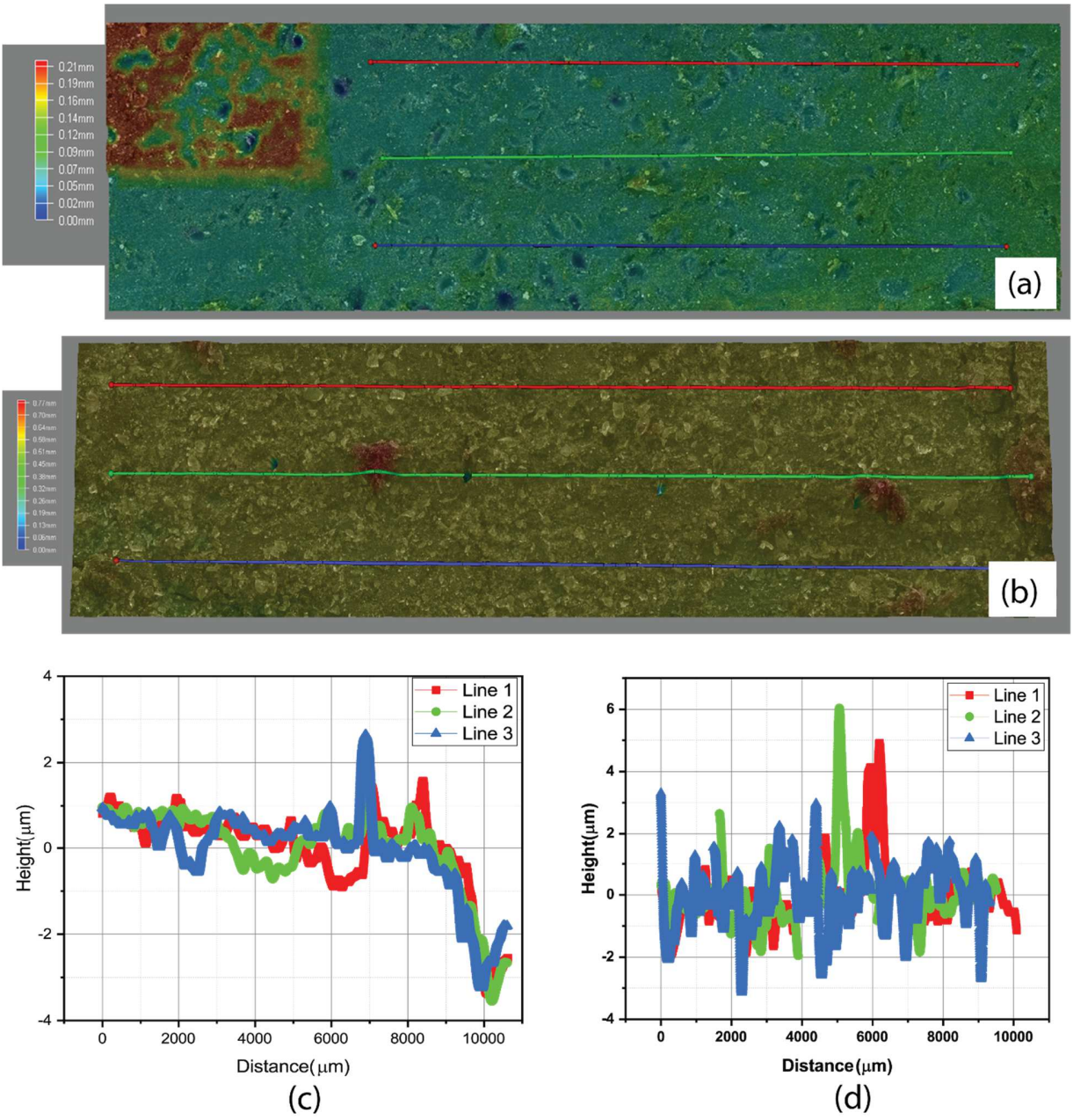

Fig. 14. (a) Surface profilometry image on which a line profile was drawn to determine the embedment depth on Ductile 2-2-3-B. (b) Surface profilometry image on which a line profile was drawn to determine the embedment depth on Reservoir 3-2-3-B. (c) Line scans showing normalized profiles of embedment depths conducted on Ductile 2-2-2-B samples. (d) Line scans showing normalized profiles of embedment depths conducted on Reservoir 3-2-2-B samples.

4. In-situ fluorescence visualization (ISFV) of fracture aperture distribution

The in-situ fluorescence images of the sample during the experiment are shown in Fig.15. The images indicate that the shale behavior was quite brittle, exhibiting severe proppant crushing. This is in spite of the relative high clay content of the sample, which categorized the shale "ductile". Most of the crushing occurred during the initial loading phase, with little additional cracking during the subsequent ~2 weeks.

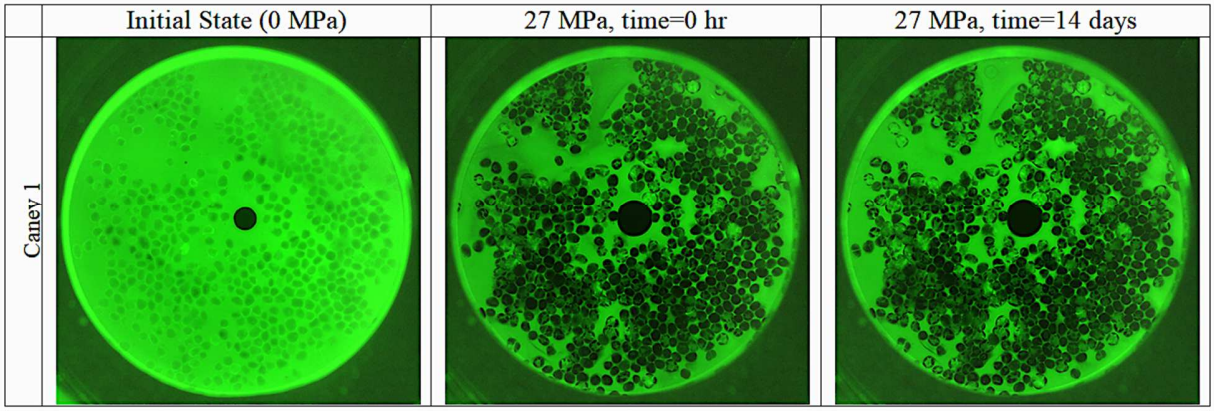

Fig. 15. UV-induced fluorescence images of the proppant and shale subjected to elevated closure stress and temperature. Severe proppant crushing resulted during the initial loading phase. During the creep compaction phase of the experiment, little additional crushing occurred. The black circle at the center of the images is a small Viton disc which was used to determine the fracture aperture changes during the initial compaction.

The initial short term (<1 hour) and the subsequent long term (up to 14 days) fracture aperture changes and additional compaction displacement are shown in Figs.16a and 16b, respectively. For the initial deformation, deformation of a small (diameter~3.2 mm) Viton disc emplaced at the center of the sample was imaged and used to determine the aperture changes. This was necessary because deformation measurements using an externally attached displacement sensor (LVDT) were affected by the deformation of the test cell and the shale sample itself. For the long-term test, however, because there were no stress changes in the system, LVDT measurements that can measure small deformations were used, assuming that the creep deformation other than the fracture was small. As Figures 17a and 17b indicate, most of the deformation occurred at very small compaction stress, less than ~2.5 MPa, and the ~70 μm of creep deformations over 14 days was also much smaller than the initial compaction. Note that because we used a rather large proppant grain size (1.0-1.5mm), the fracture aperture remained quite large (~600 μm) even when the maximum effective stress (27 MPa) was reached. For this reason, and because the proppant was sparsely distributed (~50% surface coverage), the hydraulic conductivity of the fracture remained too large to be determined accurately using this experimental setup.

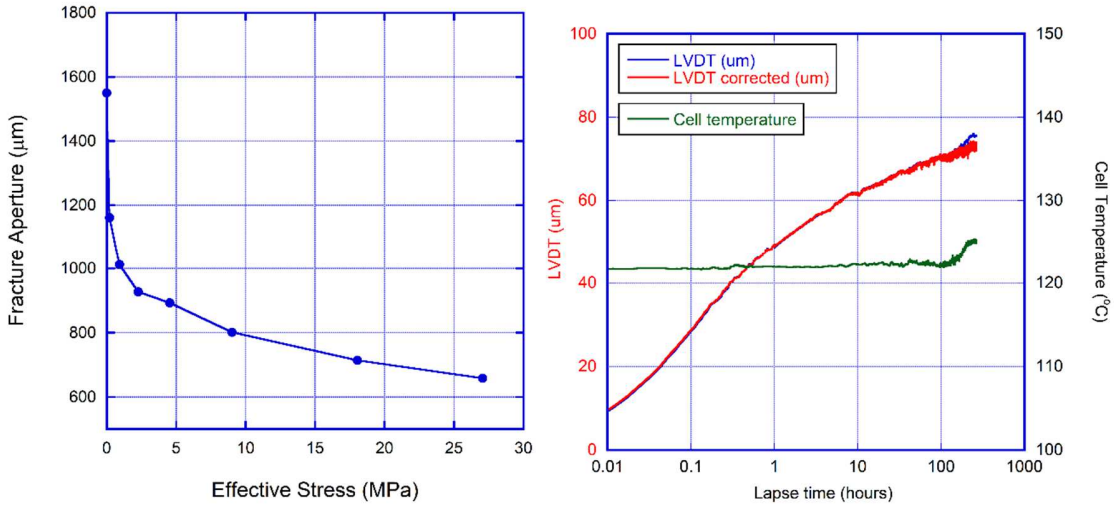

a. Initial fracture aperture changes b. Long-term creep compaction displacement

Fig.16. Initial fracture compaction (a) and long-term creep compaction (b). The initial compactions were determined from the direct aperture computed from the size of a rubber dot embedded in the fracture. For the long-term compaction measurement, malfunctioning of the temperature control system after ~10 days caused large fluctuations in sensor readings and errors.

Finally, the shale damage caused by the proppant embedment is shown in Fig.17 for the sample surface after the experiment. Unlike a highly "ductile" shale, no significant heaving of the shale matrix around indentation craters was observed. Instead, the shale matrix appeared to be pulverized around the proppant grains. (Note that the proppant and shale debris on the surface had to be cleaned off the surface during extraction of the sample from the experimental device.) This result indicates that the fracture closure in this particular Caney shale can be attributed to both crushing of proppant grains and co-produced brittle failure of the shale matrix. Although some time-dependent, viscoelastic/viscoplastic deformation was observed, its contribution to the long-term deformation of the shale is expected to be small. Instead, especially in the case of multi-layer proppant pack and only slightly propped thin fractures, clogging caused by the produced proppant and shale debris would have more significant consequences on the fracture permeability reduction.

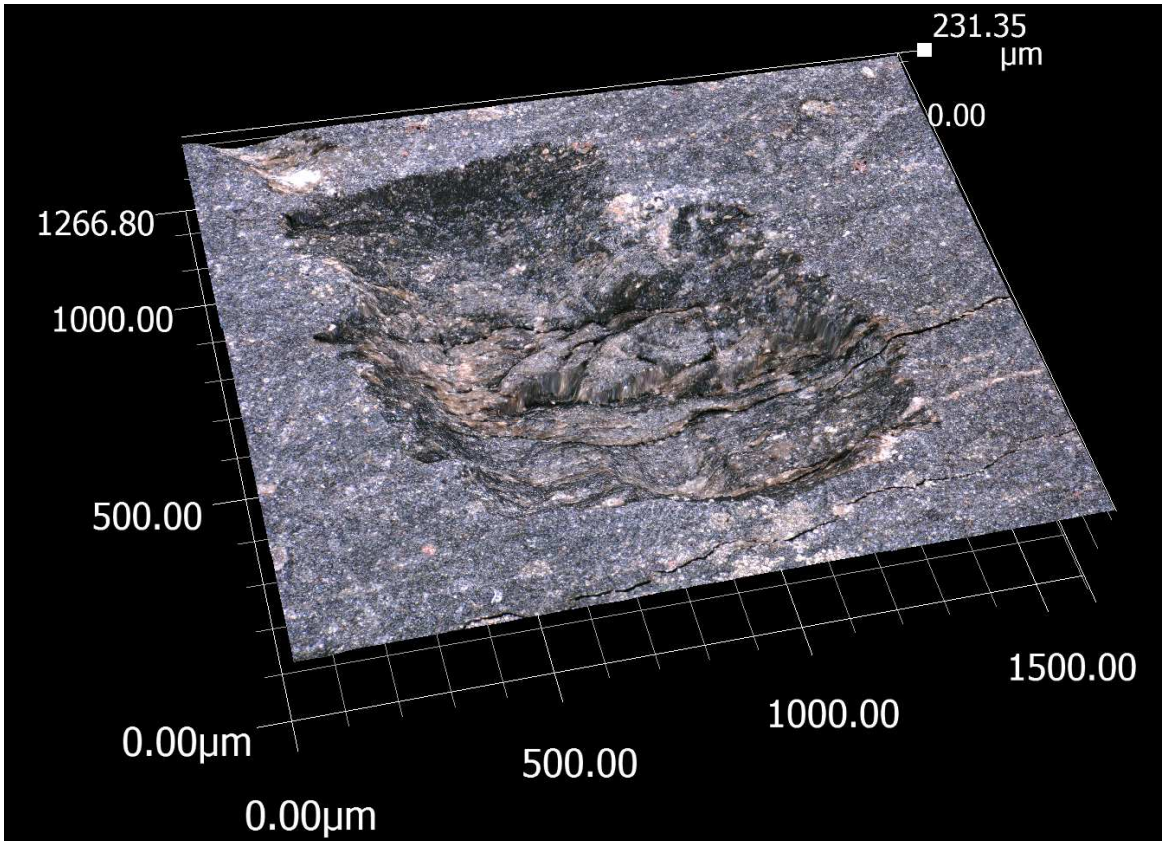

Fig.17 Photograph of the sample surface after the long-term compaction experiment. Extensive shale surface damage occurred due to proppant indentation. A close examination of the proppant craters indicate that the damage was caused by microfracturing and pulverization of the shale matrix under proppant grains, rather than plastic "heaving" of the materials around the grains.

4.6 Proppant embedment modeling

Katende et al. [5] shows proppant embedment depths of about 63µm and embedment widths of about 300 µm for a selected profile on the surface of the geological unit denoted Ductile 2 [10]. Recall that the 40/70 mesh size proppants have a pretest median size of 310µm with most grains sized in the range of 250 to 350µm. Previous model simulations in Katende et al. [10] showed that the proppant size has a significant impact on the embedment depth in addition to the force taken by an individual proppant.

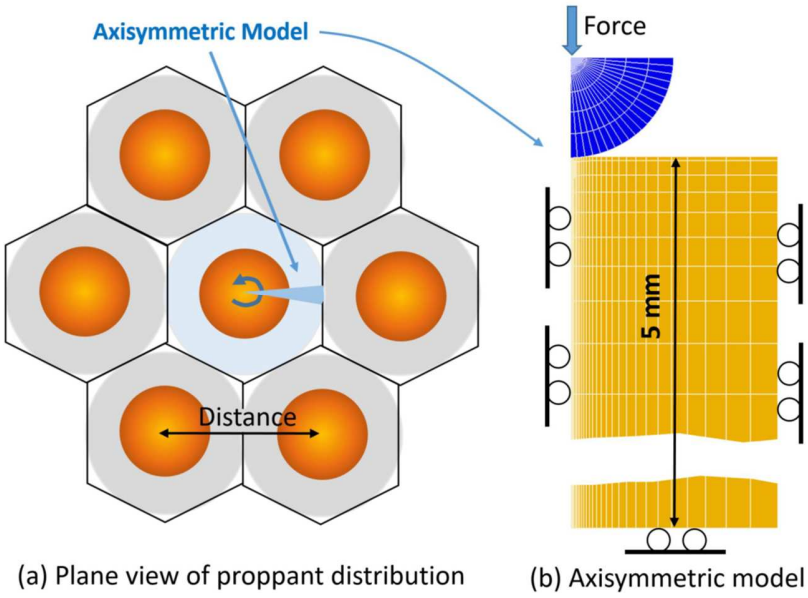

Fig. 18 Axisymmetric model for simulation of embedment of individual proppants.

The proppant embedment modeling is conducted for individual proppants using an axial symmetric model considering a spherical shape for the individual proppant (Figure 18). As in Katende et al. [10], the center-to-center distance between individual proppants is simulated by changing the radius of the axisymmetric model. Figure 19b shows the model grid, including the proppant, exposed to a vertical load, which represents the load that would be taken by an individual proppant. The load will cause the proppant to move downwards and embed into the shale. The rollers in Figure 18b illustrate boundaries where displacement is allowed parallel to the boundary surface, but no displacement is allowed normal to the boundary. In this modeling, the proppant is assumed elastic with properties corresponding to a quartz grain and is assumed to remain intact during the embedment into the softer and weaker shale sample. The shale was simulated using a Mohr-Coulomb plasticity model that has previously been demonstrated to be adequate to model elasto-plastic proppant embedment [10; 32].

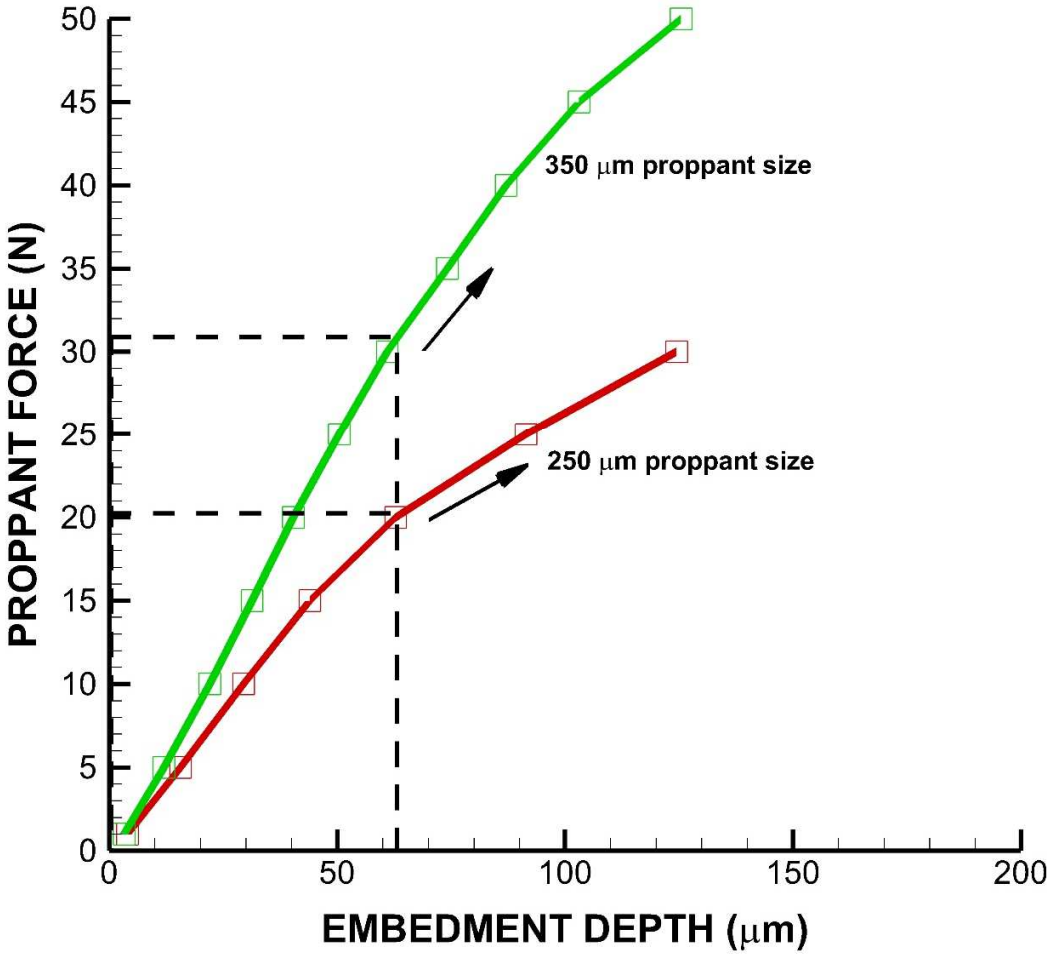

Fig. 19 Force taken by a proppant for a given embedment depth considering shale properties for the Caney Ductile 2 unit. Dashed line marks proppant force that would be required to result in a proppant embedment depth of 63μm as was experimentally observed.

Figure 19 shows simulation results of the force taken by an individual proppant for a given embedment depth using the axisymmetric model. The model simulations were conducted to determine mechanical properties representing the Caney Ductile 2 unit. These properties were derived from triaxial tests on core samples and validated by modeling micro-indentation tests in Katende et al. [10]. The properties applied for the Caney Ductile 2 unit are, young's modulus, E = 20 GPa, Poisson's ratio, ν = 0.15, cohesion, C = 22.5 MPa, and friction angle, ϕ = 25.9°. Figure 20 shows that a 350μm proppant can take more load for a given embedment depth than a smaller 250μm proppant. The dashed lines in Figure 24 indicate how much load the different sized proppant would be taking for a proppant depth of 63μm.

Figure 20 further shows simulation results of indentation profiles that match indentation profiles from Katende et al. [5] for a 250μm and 350μm proppant size. For the indentation depth of 63μm, the force taken by a 250μm proppant would be about 20 N and by a 350μm proppant it would be about 31 N (Figure 20). 32 N was applied in the modeling in Figure 19 for the 350μm proppant to achieve a slightly larger indentation depth as observed in the experiment. The force on each proppant would depend on the

stress across the sample and an average distance to surrounding proppants. The maximum stress applied in the API test was 12,000 Psi (83 MPa) and this would lead to proppant forces close to these numbers (20 and 32 N) for relatively packed proppants.

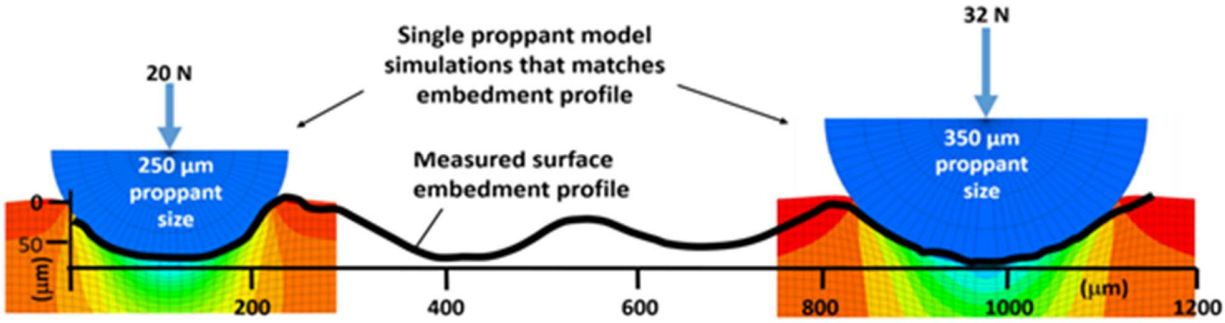

Fig. 20: Model simulation results of proppant embedment that matches the measured surface profile from Katende et al[4]. The y-axis shows the depth along the profile and the x-axis is the distance along the profiles equivalent to that in Katende et al[4].

4.7 Fracture conductivity modeling

The modeling of stress-dependent fracture conductivity of the API tests is done using a continuum model (MCC) of the proppant-pack in-between the two shale platens of each experiment. Fracture conductivity is here defined as the permeability multiplied by the fracture width and the oil-field unit for such fracture conductivity is mD-ft (milliDarcy-foot). This is a measure of the total flow transmissivity through a proppant-filled fracture. The experimental results of the API tests show that the increased stress up to the maximum of 12,000 psi (83 MPa) causes a mechanical compaction of the proppant pack (sand layer) and a significant fracture conductivity reduction. Both the proppant-pack compaction and permeability reduction are highly irreversible meaning that there is not significant rebound when stress is subsequently reduced. The initial stabilized width of the proppant-filled fracture ranged from 6.2 to 6.4 mm (0.24 to 0.25 in) at the initial normal stress of 1,000 psi (6.9 MPa). During the stress increase up to 12,000 psi (83 MPa), the fracture width was reduced by about 1.3 mm (0.051 in) to a width of about 4.8 mm (0.19 in). This implies that the proppant embedment on the order of 60 µm will have a negligible impact on the fracture closure relative to the closure caused by the compaction of the unconsolidated sand layer.

Figure 21 shows experimental and modeling results of mechanical compaction and fracture width as a function of applied stress for a set of best fit model parameters. The four different experiments show similar behavior and similar amount of compaction followed by a small rebound. This irreversible compaction is supposedly a result of grain rearrangement and grain crushing that obviously has taken place based on the experimentally determined pre- and post-proppant size distributions. In the modeling results shown by the black line in Figure 21, start at the fracture width of 6.3 mm at the initial stress of 1000-psi. The initial compaction to a fracture width of 5.7 mm at 4060-psi stress is modeled as an elastic compaction with MCC elastic compressibility parameter, kp = 0.15. At 4060-psi there is a transition to plastic compaction when the compaction starts to follow the normal consolidation line of the MCC model. This is modeled by applying the MCC pre-consolidation pressure, Po = 4060-psi, and plastic compressibility parameter p = 0.2. Finally, the elastic rebound is modeled with the MCC elastic compressibility parameter, p = 0.15, showing that the plastic compaction has induced a stiffening of the

sand layer. Such a stiffening of the sand layer may be attributed to grain crushing having taken place resulting in dense packing with crushed smaller grains occupying voids between larger grains.

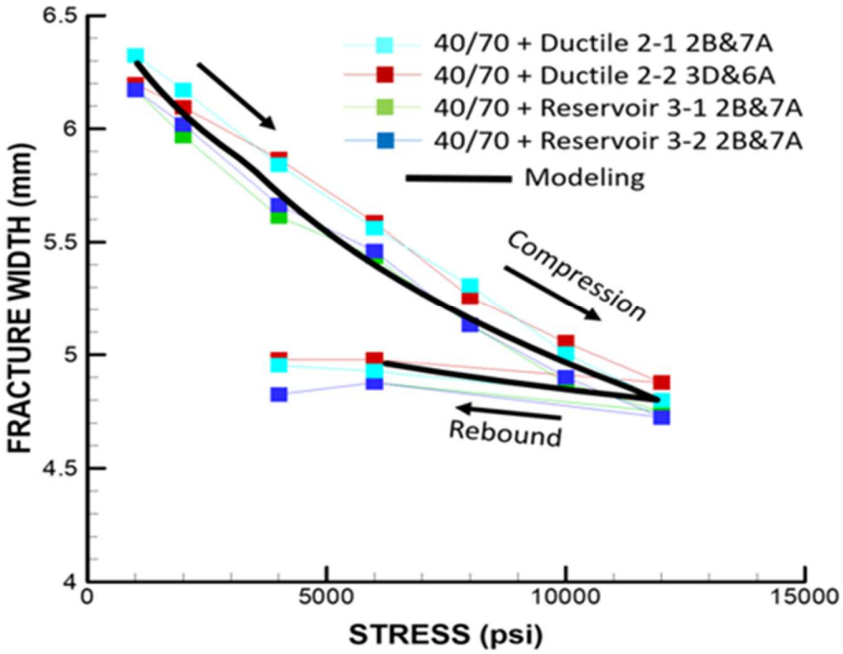

Fig. 21: Experimental and modeling results of width of proppant-filled fracture as a function of applied stress.

Following Barree et al. [36], the permeability, k, of a proppant pack at the initial stabilized state under a compressive stress 1,000 to 2,000-psi may be estimated according to the Kozeny-Carman equation considering the median particle size, dm, and porosity, ϕ, as follows:

$$k = \frac{d_m^2}{180}\frac{\phi^3}{(1-\phi)^2} \tag{3}$$

In this case we know from the experimental data that the initial proppant pack permeability ranges from 84 to 88 Darcy at 1,000 psi (6.9 MPa). We also know that the initial median grain size of the proppants is 310μm. Using a permeability of 86 Darcy ($86\text{x}10^{-12}$ m^2) and a median proppant grain size of 310μm in Equation (3) we can back-calculate a porosity of 39%. We note that in theory, the porosity for a granular medium of perfect spheres could vary between a maximum of 47% for cubical lattice structure to a minimum of 26% for a close-packed rhombohedral lattice.

Barree et al. [36] states that porosity at 1,000 to 2,000 psi initial stress state usually falls in the range of 35 to 37% meaning that the back-calculated 39% is at the higher range. However, the simulated compaction with the current model and parameters resulted in a porosity of 36.7% at 2,000 psi and decreases to 22% at the maximum stress of 12,000 psi. At the same time, we know from the experiments that proppant crushing has occurred reducing the median grain size from 310μm to about 200μm and reduced the permeability of the proppant pack to approximately 2 Darcy. Considering a porosity of 22% and a median grain size of 200μm we end up with a permeability of 4 Darcy, indicating permeability would be overestimated compared to the observed 2 Darcy permeability. The reason may be that Equation (3) is

valid for a medium of spherical grains with a uniform grain size, whereas in these experiments the compaction is accompanied by significant grain crushing that results in small sized debris that could seal bigger pores between the larger scale grains. To account for such additional permeability reduction related to the mechanical damage, we add a correction with plastic (irreversible) strain, simply on the grain size factor in Equation (3). After multiplying with the calculated fracture width, we obtain a good match to the measured fracture conductivity as shown in Figure 22. Admittedly, this match is a result of calibration of model parameters but nevertheless shows a plausible approach for modeling stress-dependent fracture conductivity of proppant-filled fractures. More research and dedicated experiments would be needed to further develop and validate such a model.

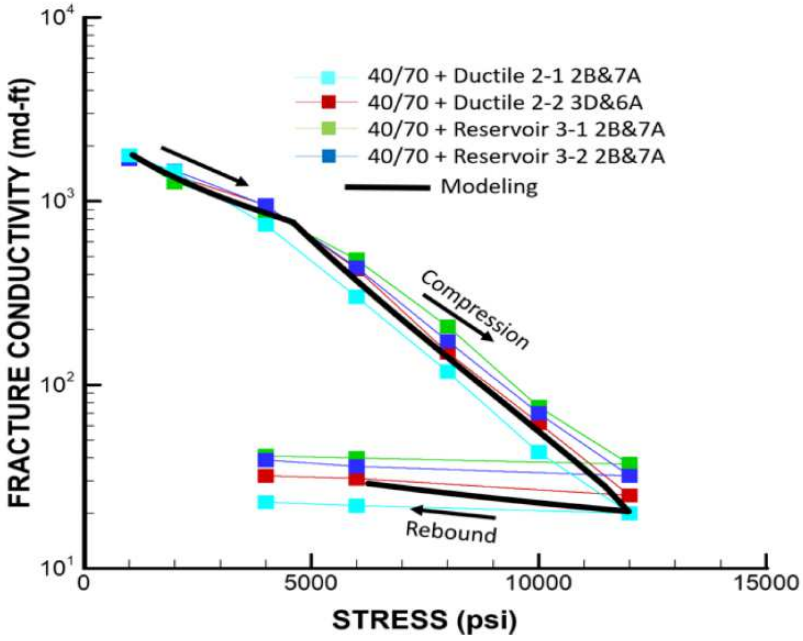

Fig. 22: Experimental and modeling results of fracture conductivity of a proppant-filled fracture as a function of applied stress.

5 Discussions

The experiments and modeling in this paper provide new data and interpretations related to the behavior of proppant-filled fractures of Caney Shale. The variation in fracture permeability, fracture width and fracture conductivity with confining stress as shown in Figures 7, 8, & 9 can be attributed to several factors, some of which are related to proppant, Caney shale samples, and experimental parameters such as pressure conditions. Proppant composition, size, its strength, and areal concentration because of flow as well as rock features, such as the rock composition and fabric, are all known to substantially impact propped fracture conductivity, as reported in literature [5]. Kainer et al. [37] compared rock characteristics and fracture conductivity in several shale plays. Various rock parameters were evaluated according to each conductivity test sample. The analyzed measurements included Young's modulus, Brinell hardness, Poisson's ratio, rock brittleness, and mineralogy. Their findings showed that increasing

surface roughness reduced the conductivity of propped fractures, while increasing Young's modulus enhanced conductivity at each closure stress. Sone and Zoback [38] demonstrated the ways in which elastic anisotropy influences shale elastic behavior. They looked at the dynamic and static elastic characteristics of different shale plays that were cored in perpendicular and parallel positions to the bedding plane configurations. These rocks' elastic characteristics varied greatly between shale formations and even within the single formation itself. The most important observation was that the elastic characteristics showed a substantial relationship with the rock fabric and mineral composition, notably the quantity of clay and organic content. Jansen et al. [39] investigated how rock mechanical characteristics affected fracture conductivity in various shale formations. Their findings showed that proppant size, concentration, strength, and rock characteristics were all important determinants in conductivity of propped fractures under varying closing pressures. They also reported that a higher Young's modulus reduced proppant embedment and improved fracture conductivity in situations in which the closure stress was increased. Similarly, Pena et al. [40] observed that a higher Young's modulus improved fracture conductivity.

Our data agrees with the literature related to rock composition impact on proppant embedment and propped fracture conductivity. For example, the effect of confining stress on fracture permeability and fracture conductivity is presented in Figures 7, 8, & 9, confirming that the Caney shale follows the same trend with other shale formations as the fracture width is dependent on confining stress. All increments in confining stress decreased the fracture width accordingly to the level of increased pressure. The same observations were reported by Zhang et al. [41] who conducted experiments on Barnett shale samples. Their conclusion was that the conductivity loss was a result of proppant embedment as the shale surface was softened after exposure to fracturing fluid during the experiment, although they did not have a quantitative data for the rock softening.

We also consider the possibility of reduced fracture conductivity and proppant embedment as evidenced in Figures 7, 8, 9, and Figure 14 to be result of the rock-fluid interaction weakening of the rock matrix. As in all rock-fluid interactions, fracturing fluid can impact the rock and indirectly affect fracture conductivity in shale formations [5]. Clay swelling, surface softening, excessive proppant embedment, and fines migration produced by fracture-surface spalling and failed proppant particles are all examples of water damage to fracture conductivity. The quantity of proppant in the fluid, level of residue in the fluid, porosity of the proppant, and proportion of residue maintained in the fracture when fluid seeps off, are the elements that cause conductivity reduction according to studies that were performed by Zhong et al. [42] & Cooke [43].

From the modeling conducted in this study, for stresses up to an expected in situ fracture closure stress of 12,000 psi, the proppant pack and fracture width was reduced by 25%, to about 4.8 mm. This reduction was a result of a highly irreversible compaction of the proppant pack that also resulted in a significant reduction in proppant pack permeability. The fracture closure and conductivity were modeled using a plastic pore-collapse model of the proppant pack, linked with a porosity permeability relation. The experiments and modeling indicate that grain rearrangement and crushing with finer debris fines filling in open spaces between the larger grains have a significant impact on the permeability. Proppant embedment of up to 60μm were observed from images of the shale platen surfaces. An embedment of about 60μm in each of the two opposite shale platens would amount to about 120m fracture closure. For the 6.3 mm width of a proppant-filled fracture, 120μm is less than 10% of the observed fracture closure of 1.4 mm. Thus, in this case proppant embedment does not have a significant direct impact on fracture conductivity changes. If, on the other hand, a monolayer of proppants is considered, a 120micro-m fracture closure

would result in a significant reduction in fracture aperture and fracture conductivity (e.g. Katende et al. [10]).

6 Conclusions

In this paper, an API standard fracture permeability test was conducted on Caney shale samples identified as reservoir and ductile. In-situ visualization tests were conducted to determine fracture compaction and long-term creep compaction. Modeling was then conducted based on API fracture conductivity experiments to understand the effect of proppant embedment and reduced fracture conductivity within the Caney Shale. From the experimental data provided and numerical modeling conducted, the following conclusions can be drawn.

1) API fracture conductivity tests showed that an increase in confining stress to 12,000 caused about two orders of magnitude decrease in fracture conductivity associated with a decrease in fracture permeability and fracture width.
2) Surface profilometry scans conducted revealed that samples with the highest proppant embedment are samples which had the highest clay content and reduced fracture conductivity.
3) Proppant compaction experiments reveal that from the ductile shale, no significant heaving of the shale matrix around indentation craters was observed but instead, the shale matrix appeared to be pulverized around the proppant grains indicating that the fracture closure in this particular Caney shale can be attributed to both crushing of proppant grains and co-produced brittle failure of the shale matrix.
4) An observed proppant embedment up to 60μm during compression to 12,000 psi in the API fracture conductivity tests could be modeled using a single proppant embedment model. In this case of an approximately 6 mm thick proppant pack, proppant embedment on the order of 60μm does not contribute significantly to the fracture conductivity loss.
5) The two orders of magnitude decrease in fracture conductivity could be modeled using a plastic pore-collapse model of the proppant pack, linked with a porosity-permeability relation. The modeling indicates that grain rearrangement and crushing with finer debris fines filling in open spaces between the larger grains have a significant impact on the permeability.
6) The API fracture conductivity tests and modeling show that the approximately 6 mm thick multilayer proppant pack can provide for substantially enhanced fracture conductivity even at the highest compressive stress of 12,000 psi. This enhanced fracture conductivity is a result of a proppant pack permeability that is several orders of magnitude higher than the permeability of the Caney shale.

Declarations of Competing Interests

The authors declare that they have no known competing interests or personal relationships that could have appeared to influence the work reported in this paper.

Acknowledgments. The authors of this paper would like to acknowledge this study was made possible by DOE Award DE-FE0031776 from the Office of Fossil Energy together with Continental Resources Inc. Funding for LBNL was provided by the U.S. Department of Energy, Office of Fossil Energy together with Continental Resources Inc, through the National Energy Technology Laboratory and Oklahoma

State University, under Award Number DE-AC02-05CH11231. The authors are grateful to Mrs. A. Rich at PropTester Inc for assistance in the experiment, and to Mr. B. Johnson and Mrs. L. Whitworth at the OSU Venture 1 Microscopy Facility for training in using the equipment. The authors also wish to acknowledge, Mr. E. Cline formerly at Chesapeake for his assistance in coring the samples, and Dr. D. Crandall from the National Energy Technology Laboratory for assistance in scanning the samples using an Industrial & Medical CT scanner. The authors are also grateful to colleagues from the Hydraulic Barrier and Materials Characterization laboratory at Oklahoma State University. The authors are also grateful to Baker Hughes for permission to use their equipment and Mr. R. Krumm for his assistance with the equipment. The authors are also grateful to Mrs. P. Reynolds for her insightful English comments on this paper.

Nomenclature

API: American Petroleum Institute

KCl: Potassium Chloride

pH: Potential Hydrogen

3D: Three dimensional

SEM: Scanning Electron Microscopy

TVDSS: True Vertical Depth Sub Sea

CT: Computed Tomography

XRD: X-ray Diffraction

kV: Kilo Volts

keV: Kilo electron Volts

XRF: X-ray Fluorescence

TOC: Total Organic Carbon

LVDT: Linear Variable Differential Transformer

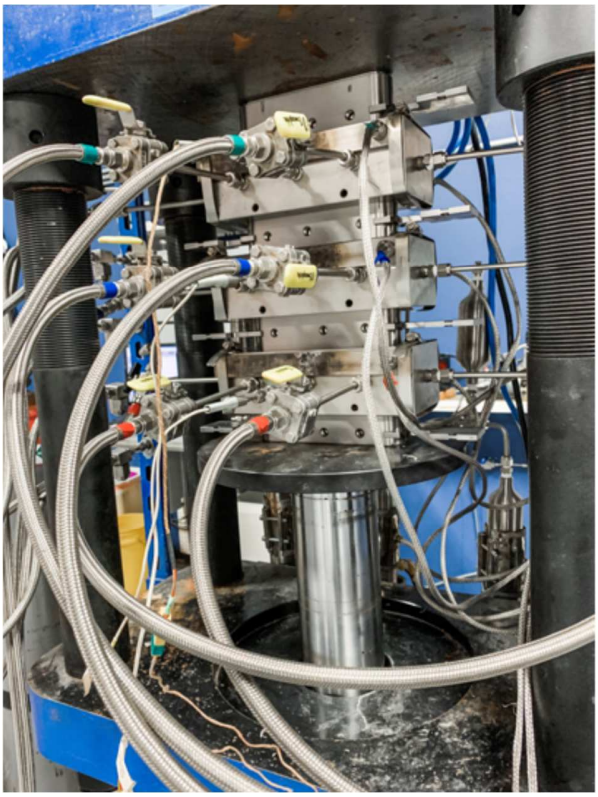

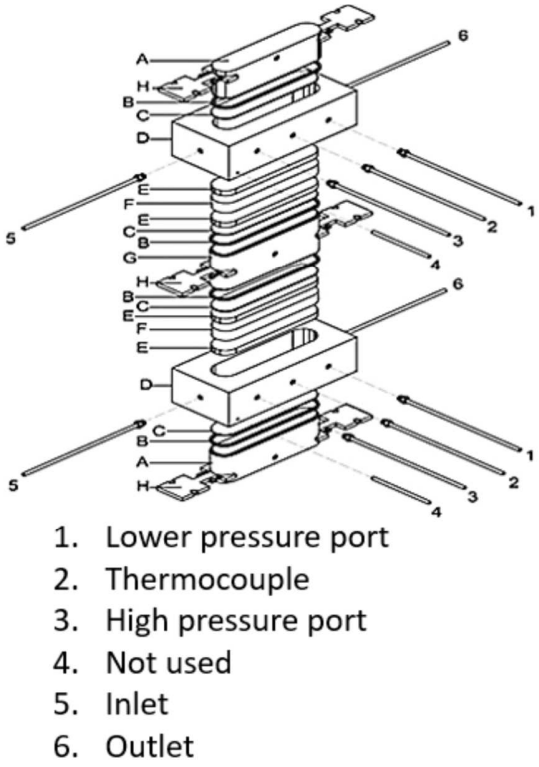

Appendix A Sample Preparation and Analysis

Fig. A1 Schematic illustration of a three-stack cell API Conductivity apparatus used in fracture conductivity testing.

Fig. A2 Schematic of the Scanning Electron Microscope set-up in the Venture I facility at Oklahoma State University Laboratory used during the sample analysis (Katende et al, 2021b).

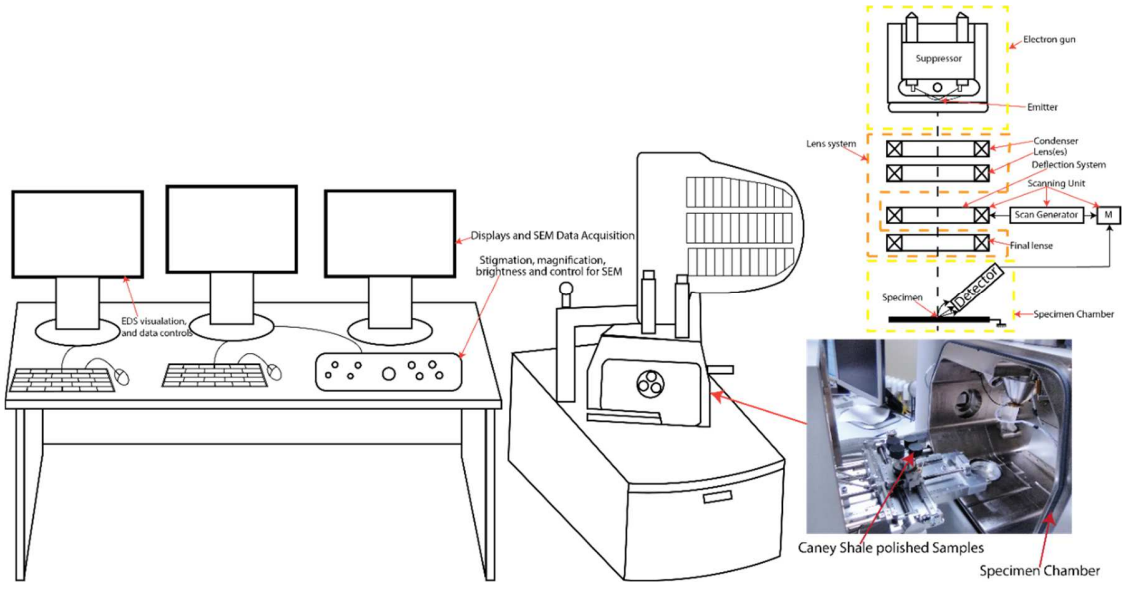

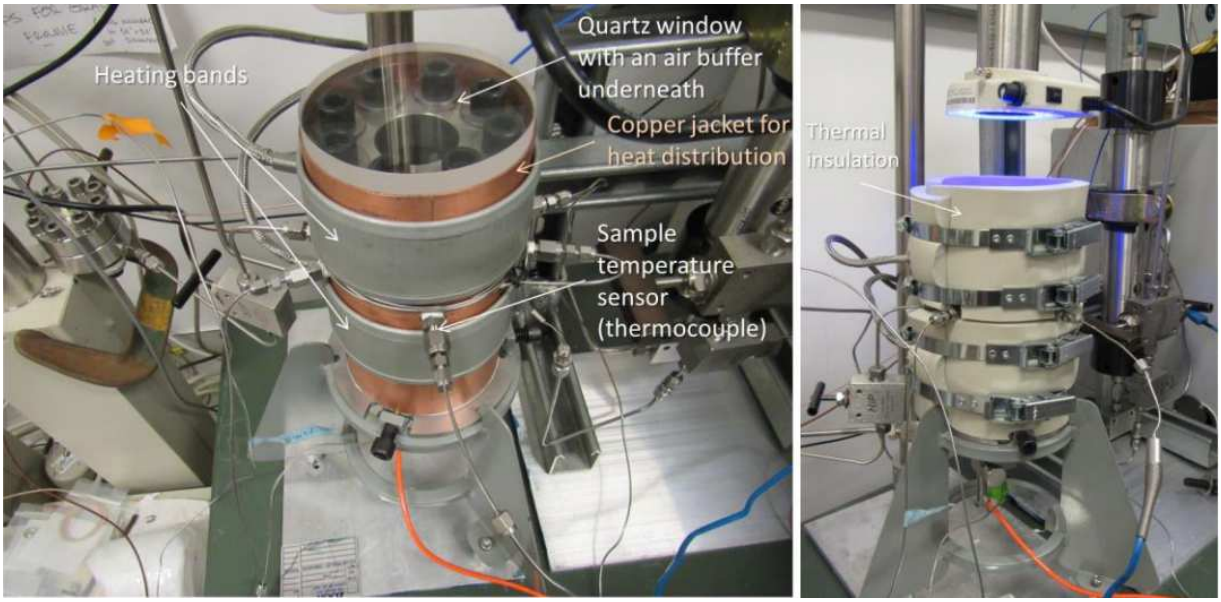

Fig. A3 Photo images of an in-situ optical visualization system for shale-proppant interaction. A large optical view window at the top of a compaction cell and fluorescence of the pore fluid induced by a UV lamp allows visualization of proppant and shale deformation under elevated stress and temperature in real time.

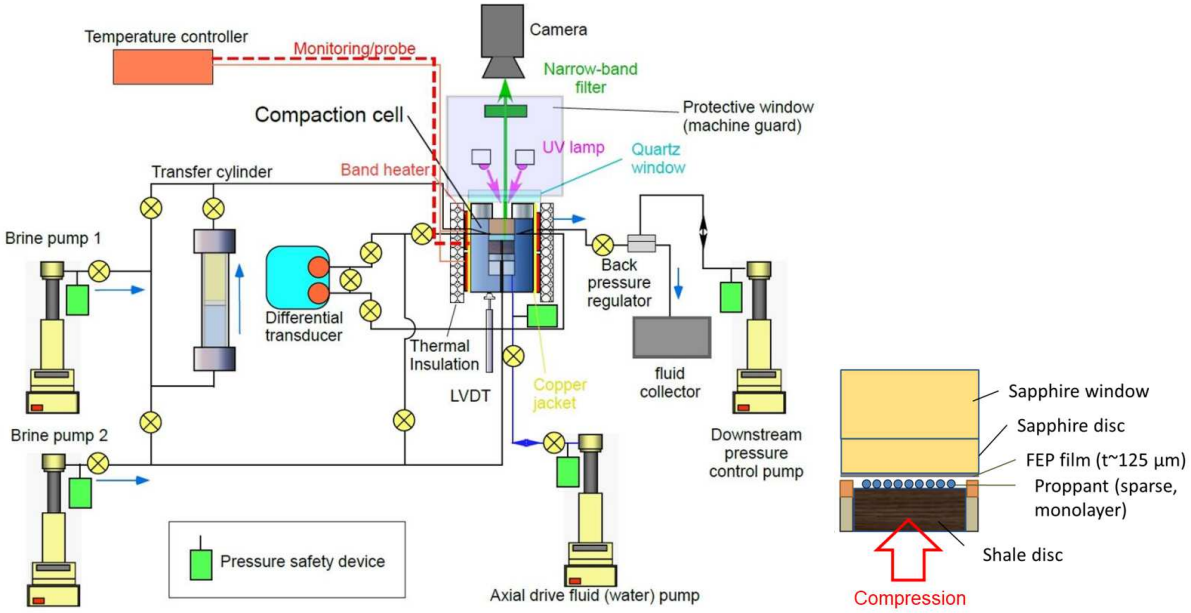

Fig. A4 Schematic view of the in-situ optical visualization system. The system allows injection and extraction of pore fluid for measuring the permeability of the fracture and a shale sample (not used in the current experiment). The internal piston applies compressive stress to the sample and the proppant, pressed against the top view window made of sapphire glass.

Appendix B: Data Presented and used in this manuscript

Table A1: Fracture conductivity data

Stress	40/70 + Ductile 2-2, 3B&6A	40/70 + Reservoir 3-1, 2B&7A	40/70 + Reservoir 3-2, 2B & 7A	40/70 + Ductile 2-1, 2B &7A
(psi)	md-ft	md-ft	md-ft	md-ft
2000	1376	1263	1466	1451
4000	952	878	948	744
6000	428	481	435	301
8000	150	208	173	118
10000	62	76	70	43
12000	25	37	32	20
6000	31	40	36	22
4000	32	41	39	23

Table A2: Fracture permeability data

Stress	40/70 + Ductile 2-2, 3B&6A	40/70 + Reservoir 3-1, 2B&7A	40/70 + Reservoir 3-2, 2B & 7A	40/70 + Ductile 2-1, 2B &7A
(psi)	[D]	[D]	[D]	[D]
2000	85	65	74	72
4000	69	48	51	39
6000	49	27	24	17
8000	23	12	10	7
10000	9	5	4	3
12000	4	2	2	1
6000	2	3	2	1
4000	2	3	2	1

Table A3: Data for particle size analysis

US Mesh	40/70 + Ductile 2-1, 2B&7A		40/70 + Ductile 2-2, 3B&6A		40/70 + Reservoir 3-2, 2B&7A		40/70 + Reservoir 3-1, 2B&7A	
	Pre Sieve	Post Sieve	Pre Sieve	Post Sieve	Pre Sieve	Post Sieve	Pre Sieve	Post Sieve
16	0	0	0	0	0	0	0	0
18	0	0	0	0	0	0	0	0
20	0	0	0	0	0	0	0	0
25	0	0	0	0	0	0	0	0
30	0.1	0.5	0.1	0.3	0.1	0.2	0.1	0.4
35	0.4	1.4	0.4	0.8	0.4	0.7	0.4	1
40	4.9	5.3	4.9	4.2	4.9	4.3	4.9	4.9
45	21.7	15	21.7	13.9	21.7	14.1	21.7	14.2
50	29.9	17.2	29.9	16.7	29.9	16.8	29.9	17.1
60	29.5	14.7	29.5	14.9	29.5	15.1	29.5	15.5
70	9.7	7.7	9.7	7.9	9.7	8	9.7	8.2
80	2.7	5.3	2.7	5.8	2.7	5.8	2.7	5.6
100	0.8	5.4	0.8	5.9	0.8	5.8	0.8	5.6
120	0.3	4.4	0.3	4.8	0.3	4.6	0.3	4.5
140	0.1	3.8	0.1	4	0.1	4.1	0.1	3.8
200	0	5.6	0	6	0	5.9	0	5.6
PAN	0	13.9	0	14.8	0	14.7	0	13.6

References

[1] M. Ahamed,M. Perera, D. Elsworth, P. Ranjith, S.Matthai, L. Dongyin, Effective application of proppants during the hydraulic fracturing of coal seam gas reservoirs: Implications from laboratory testings of propped and unpropped coal fractures, Fuel 304 (2021) 121394. doi:10.1016/j.fuel.2021.121394.

[2] G. Jianming, Q. Zhen, Z. Caineng, W. Hongyan, S. Zhensheng, An integrated assessment system for shale gas resources associated with graptolites and its application, Applied Energy 262 (114524) (2020) 1–9. doi:10.1016/j.apenergy.2020.114524.

[3] S. Kadoshin, T. Nishiyama, T. Ito, The trend in current and near future energy consumption from a statistical perspective, Applied Energy 67 (4) (2000) 407–417. doi:10.1016/S0306-2619(00)00033-7.

[4] N. J. Welch, M. Meng, W. Li, L. P. Frash, M. Wigand, J. W. Carey, Shear Induced Matrix Damage and Micro-Fracturing in Oil Shale, Paper presented at the SPE/AAPG/SEG Unconventional Resources Technology Conference, Houston, Texas, USA, June 2022., 2022, pp. 1–10. doi:10.15530/urtec-2022-3709758.

[5] A. Katende, L. O'Connell, A. Rich, J. Rutqvist, M. Radonjic., A comprehensive review of Proppant embedment in shale reservoirs : Experimentation, modeling and future prospects, Journal of Natural Gas Science and Engineering 95 (104143) (2021) 1–29. doi:10.1016/j.jngse.2021.104143.

[6] H. Sun, B. He, H. Xu, F. Zhou, M. Zhang, H. Li, G. Yin, S. Chen, X. Xu, B. Li, Experimental Investigation on the Fracture Conductivity Behavior of Quartz Sand and Ceramic Mixed Proppants, ACS Omega 7 (12) (2022) 10243–10254. doi:10.1021/acsomega.1c06828.

[7] M. Maslowski, M. Labus, Preliminary Studies on the Proppant Embedment in Baltic Basin Shale Rock, Rock Mechanics and Rock Engineering (2021) 1–16. doi:10.1007/s00603-021-02407-0.

[8] API-RP19D, Recommended practice for measuring the long-term conductivity of proppants.

[9] API-RP-19C, Measurement of Properties of Proppants Used in Hydraulic Fracturing and Gravel-packing Operations, American Petroleum Institute.

[10] A. Katende, J. Rutqvist, M. Benge, A. Seyedolali, A. Bunger, J. O. Puckette, A. Rhin,M. Radonjic, Convergence of micro-geochemistry and micro-geomechanics towards understanding proppant shale rock interaction: A Caney shale case study in southern Oklahoma, USA, Journal of Natural Gas Science and Engineering 96 (2021) 104296. doi:10.1016/j.jngse.2021.104296.

[11] C. Fredd, S. McConnell, C. Boney, K. England, Experimental Study of Hydraulic Fracture Conductivity Demonstrates the Benefits of Using Proppants, Paper presented at the SPE Rocky Mountain Regional/Low-Permeability Reservoirs Symposium and Exhibition, Denver, Colorado, March 2000., 2000, pp. 1–14. doi:10.2118/60326-MS.

[12] J. Wang, D. Elsworth, Role of proppant distribution on the evolution of hydraulic fracture conductivity, Journal of Petroleum Science and Engineering 166 (2018) 249–262. doi:10.1016/j.petrol.2018.03.040.

[13] W. Zheng, S. C. Silva, D. D. Tannant, Crushing characteristics of four different proppants and implications for fracture conductivity, Journal of Natural Gas Science and Engineering 53 (2018) 125–138. doi:10.1016/j.jngse.2018.02.028.

[14] R. Allen, Stratigraphy, mountain building and complex geological structures of the Ardmore Basin, The Shale Shaker 11 (2000) 1–12.

[15] W. J. Perry, Tectonic Evolution of the Anadarko Basin Region, Oklahoma, U.S. Geological Survey Bulletin 1866-A (1989) 1–28.

[16] G. R. Keller, E. G. Lidiak, W. K. Hinze, L. W. Braile, The role of Rifting in the Tectonic Development of the Midcontinent, U.S.A, Tectonophysics 94 (1983) 391–412. doi:10.1016/B978-0-444-42198-2.50028-6.

[17] S. Feinstein, Subsidence and Thermal History of Southern Oklahoma Aulacogen: Implications for Petroleum Exploration, The American Association of Petroleum Geologists Bulletin 65 (12) (1981) 2521–2533. doi:10.1306/03B599F9-16D1-11D7-8645000102C1865D.

[18] D. R. Lowe, Regional Controls on Silica Sedimentation in the Ouachita System, GSA Bulletin 86 (8) (1975) 1123C1127.
[19] J. L. Evans, Major Structural Features of the Anadarko Basin, Tulsa Geological Society 1 (1) (1979) 97–114.
[20] H. D. Wang, R. P. Philp, Geochemical Study of Potential Source Rocks and Crude Oils in the Anadarko Basin, Oklahoma, AAPG Bulletin 81 (2) (1997) 249C275. doi:10.1306/522B42FD-1727-11D7-8645000102C1865D.
[21] B. J. Cardott, Overview of Unconventional Energy Resources of Oklahoma, Oklahoma Geological Survey (2017) 1–10.
[22] P. J. Kamann, Surface-to-subsurface Correlation and Lithostratigraphic Framework of the Caney Shale (Including the "mayes" Formation) in Atoka, Coal, Hughes, Johnston, Pittsburg, and Pontotoc Counties, Oklahoma, Master's thesis, Oklahoma State University, Boone Pickens School of Geology 105 Noble Research Center Stillwater, OK 74078 (2006).
[23] T. J. Paronish, R. Schmitt, J. E.Moore, D. Crandall, A. Rihn, J. Renk, C. Doughty, A. Bunger, Y.Wang, A. Katende, A. Seyedolali, J. Puckette, M. Radonjic, Computed tomography scanning and geophysical measurements of the caney shale formation from the tomaney# 1-35- 34-27 well 1. doi:10.2172/1812176.
[24] G. Awejori, F. Xiong, A. Katende, M. Radonjic, L. Whitworth, T. Paronish, Fluid Induced Elemental and Mineralogy Alterations of Caney Shale, Paper presented at the 56th U.S. Rock Mechanics/Geomechanics Symposium, Santa Fe, New Mexico, USA, June 2022. Paper Number: ARMA-2022-0763, 2022, pp. 1–11. doi:10.56952/ARMA-2022-0763.
[25] S. Nakagawa, E. Borglin, Laboratory In-Situ Visualization of Long-Term Fracture Closure and Proppant Embedment in Brittle and Ductile Shale Samples, 53rd US RockMechanics/Geomechanics Symposium held in New York, NY, USA, 23 June 2019, 2019, pp. 1–8.
[26] J. Rutqvist, An overview of TOUGH-based geomechanics models, Computers & Geosciences 108 (2017) 56–63. doi:10.1016/j.cageo.2016.09.007.
[27] J. Rutqvist, Status of the TOUGH-FLAC simulator and recent applications related to coupled fluid flow and crustal deformations, Computers & Geosciences 108 (2011) 56–63. doi:10.1016/j.cageo.2010.08.006.
[28] Itasca, FLAC3d v5.0, Fast Lagrangian Analysis of Continua in 3 Dimensions, Users Guide.
[29] K. Pruess, C. Oldenburg, G. Moridis, Report LBNL-43134. Lawrence Berkeley National Laboratory, Berkeley, CA, USA, User Guide 2.1.
[30] K. H. Roscoe, J. B. Burland, On the generalized stress-strain behavior of wet clay., In Engineering plasticity. (1968) 535–609.
[31] C. Chang, M. D. Zoback, Viscous creep in room-dried unconsolidated Gulf of Mexico shale (II): Development of a viscoplasticity model , Journal of Petroleum Science and Engineering 72 (2010) 50– 55. doi:10.1016/j.petrol.2010.03.002.
[32] M. Voltolini, J. Rutqvist, T. Kneafsey, Coupling dynamic in situ X-ray micro-imaging and indentation: A novel approach to evaluate micromechanics applied to oil shale, Fuel 300 (2021) 120987. doi:10.1016/j.fuel.2021.120987.
[33] M. Radonjic, G. Luo, Y. Wang, M. Achang, J. Cains, A. Katende, J. Puckette, M. Grammer, G. E. King, Integrated Microstructural Characterisation of Caney Shale, OK, Unconventional Resources Technology Conference, 2020, pp. 1–18. doi:10.15530/urtec-2020-2947.
[34] R. M. Holt, E. Fjaer, J. F. Stenebraten, O.-M. Nes, Brittleness of shales: Relevance to borehole collapse and hydraulic fracturing, Journal of Petroleum Science and Engineering 131 (2015) 200–209. doi:10.1016/j.petrol.2015.04.006.
[35] M. Much, G. Penny, Long-Term Performance of Proppants Under Simulated Reservoir Conditions, Paper presented at the SPE/DOE Joint Symposium on Low Permeability Reservoirs, Denver, Colorado, May 1987., 1987, pp. 1–10. doi:10.2118/16415-MS.
[36] R. D. Barree, R. J. Duenckel, B. T. Hlidek, Proppant Sieve Distribution - What Really Matters?, Society of Petrolem Engineering, 2019. doi:10.2118/194382-MS.

[37] C. Kainer, D. Guerra, D. Zhu, A. D. Hill, A comparative analysis of rock properties and fracture conductivity in shale plays, Society of Petroleum Engineering, 2017. doi:10.2118/184877-MS.
[38] H. Sone, M. D. Zoback, Mechanical properties of shale-gas reservoir rocks 0309 Part 1: Static and dynamic elastic properties and anisotropy, Geophysics 78 (5) (2013) D381CD392. doi:10.1190/geo2013-0050.1.
[39] T. Jansen, D. Zhu, A. D. Hill, The Effect of Rock Mechanical Properties on Fracture Conductivity for Shale Formations, Paper presented at the SPE Hydraulic Fracturing Technology Conference, The Woodlands, Texas, USA, February 2015. Paper Number: SPE-173347-MS, 2015, pp. 1–21. doi:10.2118/SPE-173347-MS.
[40] P. P. Pena, D. Zhu, A. D. Hill, The Effect of Rock Properties on Fracture Conductivity in the Marcellus Shale, Paper presented at the SPE Asia Pacific Hydraulic Fracturing Conference, Beijing, China, August 2016. Paper Number: SPE-181867-MS, 2016, pp. 1–19. doi:10.2118/181867-MS.
[41] J. Zhang, L. Ouyang, D. Zhu, A. D. Hill, Experimental and numerical studies of reduced fracture conductivity due to proppant embedment in the shale reservoir, Journal of Petroleum Science and Engineering 130 (2015) 37–45. doi:10.1016/j.petrol.2015.04.004.
[42] Y. Zhong, E. Kuru, H. Zhang, J. Kuang, J. She, Effect of Fracturing Fluid/Shale Rock Interaction on the Rock Physical and Mechanical Properties, the Proppant Embedment Depth and the Fracture Conductivity, Rock Mechanics and Rock Engineering 52 (2018) 1011C1022. doi:10.1007/s00603-018-1658-z.
[43] C. E. Cooke, Effect of Fracturing Fluids on Fracture Conductivity, Paper Number: SPE-5114-PA, 1975, pp. 1–10. doi:10.2118/5114-PA.